Precambrian Research 431 (2025) 107946

Contents lists available at ScienceDirect

Precambrian Research

journal homepage: www.elsevier.com/locate/precamres

Research Paper

Petrogenesis of the Paleoproterozoic Liuying hornblendite arc cumulates and implications for the tectonic evolution of the northern North China Craton

Wen-Mei Liu [a,b], Jian-Ping Zheng [a,*], Bernard Charlier [b], Qiang Ma [a], Timothy Kusky [a], Hong-Kun Dai [a]

[a] School of Earth Sciences, State Key Laboratory of Geological Processes and Mineral Resources, China University of Geosciences, Wuhan 430074, China
[b] Department of Geology, University of Liege, Liege B-4000, Belgium

ARTICLE INFO

Keywords:
Paleoproterozoic
North China Craton
Hornblendite
Continental arc
Lithospheric mantle modification

ABSTRACT

Understanding the Paleoproterozoic configuration of the northern North China Craton (NCC) is crucial for reconstructing its Precambrian tectonic history. This study integrates geological field observations, petrological data, U-Pb geochronology, and Lu-Hf isotopic analysis of zircons, alongside mineral and whole-rock geochemistry, including Sr-Nd isotopes from the Liuying ultramafic complex in Hebei Province. Our goal is to enhance the understanding of the tectonic history of the craton's northern margin. The complex is composed of hornblendite and plagioclase hornblendite, showing igneous cumulate texture. Zircon U-Pb data from the ultramafic complex define three distinct groups of ages: 2211–2343 Ma, 1761–1999 Ma, and 246–310 Ma, corresponding to magma crystallization and metamorphism resulted from crustal thermal events. The major elements of rocks align with the differentiation trend of hydrous arc magmas. They display characteristics of enrichment in large ion lithophile elements and depletion in high field strength elements. Fractional crystallization of arc magmas with H_2O of 7.3–8.1 wt% at middle-lower crust depths (18–23 km) and 966–996 °C formed amphibole-enrichment arc cumulates. The zircon $\varepsilon_{Hf}(t)$ values (–5.96 to + 9.05) are decoupled from enriched Sr-Nd isotopic compositions ($(^{87}Sr/^{86}Sr)_i = 0.704185$–$0.705932$, $\varepsilon_{Nd}(t) = -14.6$ to -5.68, $(^{87}Sr/^{86}Sr)_{amp} = 0.705110$–$0.705846$), suggesting a subduction-modified mantle source, incorporating 5–10 % subduction slab-derived melts and fluids. The northern part of the NCC was a continental arc above a paleo-subduction zone on a scale similar to the modern Andes at ca. 2.2 Ga. The oceanic slab subduction between the craton and the Siberian segment resulted in partial melting of metasomatized mantle wedge to form Paleoproterozoic hornblendite arc cumulates.

1. Introduction

The North China Craton (NCC), one of the major Precambrian blocks on our planet, has Archean- and Paleoproterozoic basements (Song et al., 1996; Zheng et al., 2004) covering an area of over 300,000 square kilometers. Establishing the Precambrian tectonic evolution of the craton can help to constrain the tectonic framework and evolution of the Columbia supercontinent (Zhao et al., 2002) and investigate early Earth plate tectonics including subduction and large-scale horizontal crustal motions (Korenaga, 2013; Cawood et al., 2018; Yin et al., 2020; Zhong et al., 2021; Sun et al., 2021). The craton's Precambrian tectonic processes were generally interpreted as protracted subduction followed by ca. 1.85 Ga continent–continent collision (e.g., Wilde et al., 2002; Zhao et al., 2005; Faure et al., 2007; Zhang et al., 2007; Trap et al., 2012); or cycles of subduction, collision, and rifting (e.g., Kusky and Li, 2003; Kusky et al., 2007, 2016; Wan et al., 2015, 2020; Wang et al., 2017, 2019; Wu et al., 2018; Zhong et al., 2021; Zhai et al., 2021; Wei et al., 2023). Despite decades of prolific research which has generated a wealth of geologic data, no consensus has been reached on the Precambrian tectonic evolution of the craton (e.g., Kusky, 2011, Kusky et al., 2016; Wan et al., 2015; Wang et al., 2017; Zhang et al., 2012a; Zhang et al., 2012b; Ning et al., 2022; Zhang et al., 2023), which is partially due to an inadequate understanding of the Paleoproterozoic tectonic history of the northern NCC (Fig. 1).

Previous studies suggested that the northern NCC was an Andean-type continental margin that collided with the Siberian segment of the

---

* Corresponding author.
E-mail address: jpzheng@cug.edu.cn (J.-P. Zheng).

https://doi.org/10.1016/j.precamres.2025.107946
Received 18 March 2025; Received in revised form 19 July 2025; Accepted 10 October 2025

Columbia Supercontinent during Paleoproterozoic (2.3–1.85 Ga) (Kusky et al., 2016; Wu et al., 2018, 2023; Wan et al., 2020; Sun et al., 2021; Zhang et al., 2023). However, direct geological records of Paleoproterozoic continental arc are rare in the northern NCC, which inhibits our understanding about the tectonic history of the craton's northern margin. Neoarchean to Paleoproterozoic amphibole-enriched cumulates (e.g., hornblendite, garnet amphibolite, diorite) constitute a rare but genetically important occurrence within the arc systems and their genesis holds key information for monitoring the evolution of mantle source and the geodynamic processes along ancient convergent plate margins (Smith, 2014; Daczko et al., 2016; Triantafyllou et al., 2018).

In this contribution, systematic geological field and petrological observations, U-Pb geochronology and Lu-Hf isotope of zircons, mineral and whole-rock geochemistry including Sr-Nd isotopes are presented from newly identified hornblendites in the northern Hebei Province, northern margin of the NCC. Our study suggests that the hornblendite arc cumulates emplaced at Paleoproterozoic (2.2 Ga) and formed via fractional crystallization of hydrous arc magmas. The ultramafic cumulates derived from a metasomatized mantle source mixed subduction slab-derived fluids and melts. We propose that the northern part of the North China Craton was a continental arc above a paleo-subduction zone on a scale similar to the modern Andes at ca. 2.2 Ga. The oceanic slab subduction between the craton and the Siberian segment resulted in partial melting of metasomatized mantle wedge to form Paleoproterozoic hornblendite arc cumulates.

2. Geological background

The NCC is surrounded by several Phanerozoic subduction and collision zones, including the Central Asian Orogenic Belt to the north, the Qinling-Dabie Belt to the south, the Qilian Orogen to the west, and the Su-Lu and Jiao-Liao-Ji Orogens to the east (Fig. 1, e.g., Xiao et al., 2015). The basement rocks of the craton are primarily composed of Archean- and Paleoproterozoic amphibolite to granulite facies gneisses, which are unconformably overlain by Meso- to Neo-Proterozoic sedimentary rocks. The NCC is traditionally divided into two major Archean-Proterozoic blocks: the Eastern Block and Western Block, separated by the ~ 1,800-km-long north-trending Neoarchean-Paleoproterozoic Central Orogenic Belt (COB) or Paleoproterozoic Trans-North China Orogen (TNCO) (Kusky and Li, 2003; Zhao et al., 2005; Kusky et al., 2007, Kusky et al., 2016). The Eastern Block contains 3.8–2.6 Ga gneiss and greenstone belts, along with associated metasedimentary sequences (e.g., Zhao et al., 2005; Kusky et al., 2016). The Western Block is composed of the Khondalite Belt, Ordos Block, and Yinshan Blocks, and is covered by thick Mesozoic to Quaternary sediments (Kusky and Mooney, 2015).

The collisional ages and tectonic framework between the Eastern Block and Western Block exhibit a complex and controversial evolutionary history, involving arc, micro-continent, or continental block convergence and cratonization processes from the late Neoarchean to the Paleoproterozoic. The evolutionary history of the NCC is generally described by one of two models. Zhao et al. (2002, Zhao et al., 2005, Zhao et al., 2012), Wilde et al. (2002), and Sun et al. (2019) proposed that the NCC was formed by the suturing of Eastern and Western Blocks across the TNCO around 1.85 Ga. In this context, convergence between the Western Block and Eastern Block was facilitated by east-dipping subduction, with their collision occurred at ca. 1.85 Ga along the TNCO (e.g., Zhang et al., 2007; Zhao et al., 2005; Zhao et al., 2012). The Western Block resulted from the collision between the Yinshan Block and Ordos Block at ca. 1.95 Ga along the Paleoproterozoic Khondalite Belt, which underwent a medium to high-pressure granulite-facies metamorphic event (Zhao et al., 2001, Zhao et al., 2002, Zhao et al., 2005, Zhao et al., 2012). Before the collision between the Eastern Block and Western Block at ca. 1.85 Ga, a long-lived (~700 Myr) continental margin existed west of the Eastern Block during the late Neoarchean to Paleoproterozoic (Zhao et al., 2006, Zhao et al., 2012).

Alternatively, the accretion of a ribbon continent with a continental margin arc developed in northern NCC by 2.3 Ga (Kusky et al., 2007; Kusky and Santosh, 2009; Wu et al., 2022). The Eastern Block of the NCC, composed of older accreted arcs, collided with the Wutai/Fuping arc of the COB at ca. 2.5 Ga, and the Inner Mongolia-Northern Hebei Orogen (IMNHO) formed along the northern NCC between 2.3 and 1.8 Ga (e.g., Kusky and Li, 2003; Kusky et al., 2016; Wang et al., 2013, Wang et al., 2017). After 2.3 Ga, the northern margin of the NCC became an active continental margin with southward subduction (in present coordinates), with far-field effects felt across the craton, comparable in scale to the modern Andes (Kusky et al., 2016). At ca. 1.85 Ga, the northern NCC collided with the Siberian segment of the Columbia

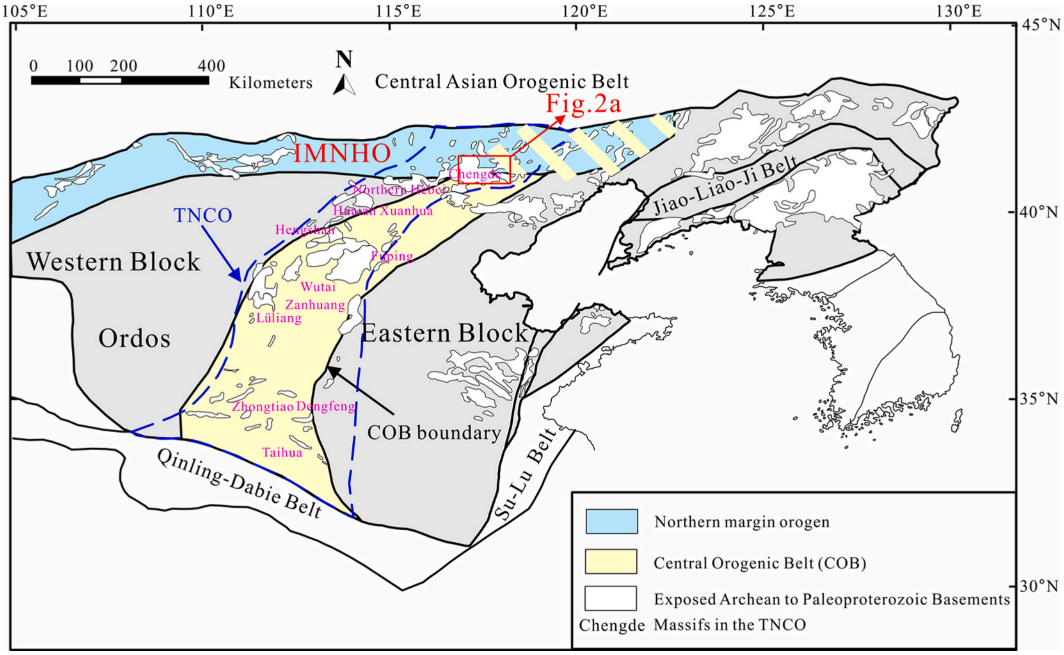

Fig. 1. (a) Tectonic framework of the North China Craton and location of studied area (modified from Zhang et al., 2023).

Supercontinent (Kusky and Santosh, 2009; Kusky et al., 2016) triggering metasomatism across the craton on a scale similar to that of the modern Tibetan plateau (Kusky et al., 2016).

The tectonic framework of the northern NCC is also debated, with competing models that differ with, but are related to the previously discussed groups of models. The northern NCC encompasses the Khondalite Belt and Yinshan Block (e.g., Kusky et al., 2007, 2016; Peng et al., 2014; Wan et al., 2015; Wang et al., 2017). A molasse basin older than 1.9 Ga separates the Khondalite Belt from the Yinshan microcontinent (Kusky et al., 2016). The Yinshan Block coalesced with the Ordos Block to the southeast along the Khondalite Belt at ca. 1.92 Ga, comprising what is termed the Western Block (e.g., Santosh et al., 2007a, 2007b; Zhao et al., 2005). Archean rocks of the northern NCC are primarily divided into the Paleoarchean Xinghe Group (granulite, biotite plagiogneiss, and quartzite), the Mesoarchean Wulashan Group (amphibole gneiss, granulite, quartzite, marble, and biotite schist), and the Neoarchean Sertengshan Group (biotite amphibolite, magnetite-quartzite, quartz schist, marble, and biotite hornfels) (Wu et al., 2023). These rocks are conformably overlain by the Neoarchean-Paleoproterozoic Baoyintu Group, Hongqiyingzi Group, and rocks of the Khondalite belt. The Paleoproterozoic Baoyintu Group is composed of upper greenschist to lower amphibolite-facies metamorphic rocks, featuring a basal unit of quartzite, marble, and schist interlayered with lamellar marble lenses. The Neoarchean-Paleoproterozoic Hongqiyingzi Group mainly comprises quartz dioritic, tonalitic, and granodioritic gneisses, as well as granodiorite, monzogranite, syenogranite intrusions, and amphibolite (Liu et al., 2019).

3. Field relationships and sample petrography

The Liuying ultramafic complex, located in northern Hebei Province within the northern NCC, exhibits an east–west shape elongation and is situated along the southern margin of the Damiao-Hongshila Fault (Fig. 2a). This complex comprises three distinct ultramafic unites: I, II, and III. (Fig. 2b). Locally, the complex displays lens-like features, having been magmatically emplaced at the contact with the host Hongqiyingzi

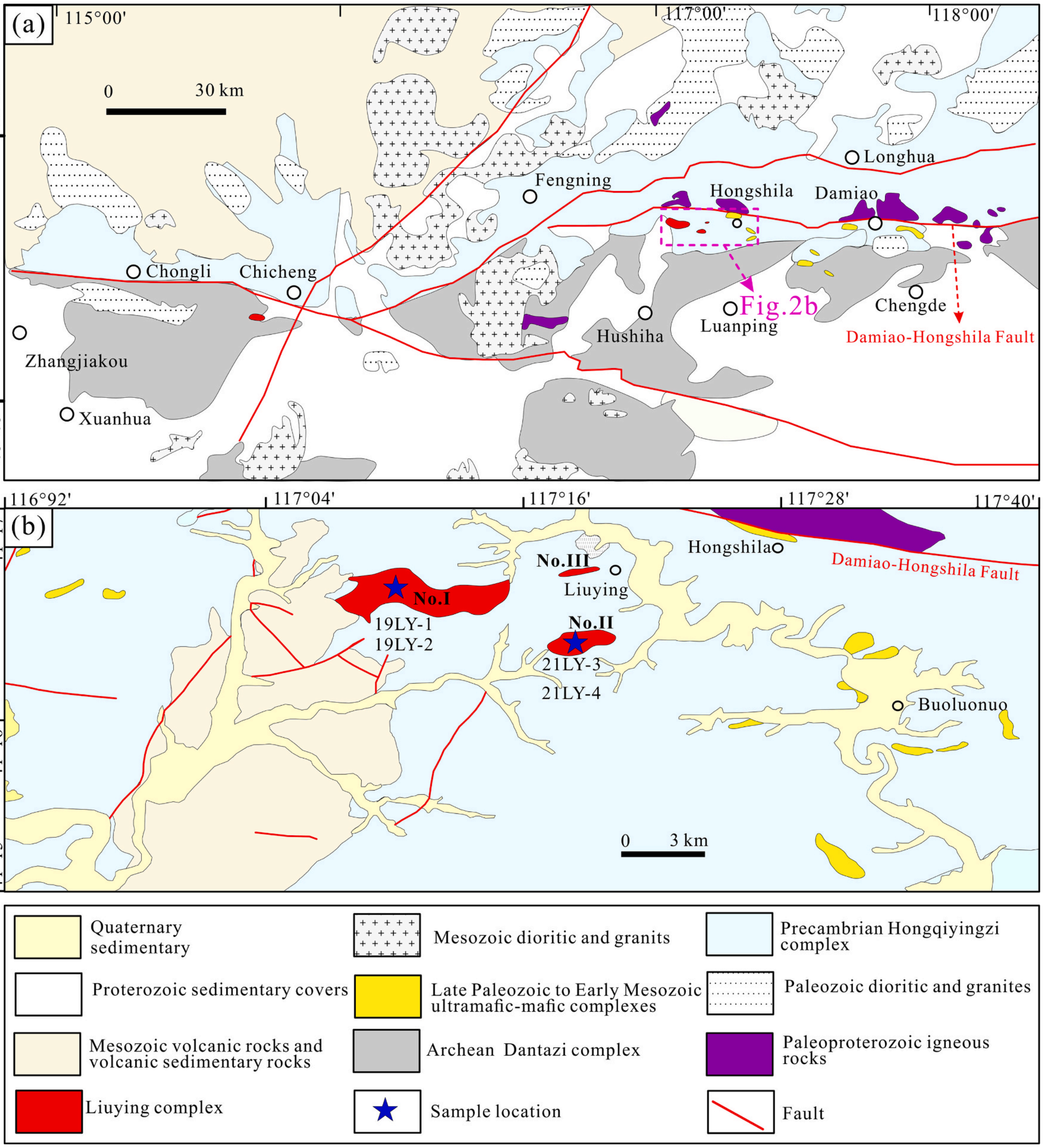

Fig. 2. (a) Geological sketch map of the Chengde region (modified from Liu et al., 2019); (b) Geological sketch map of the Liuying ultramafic complex. The sample locations of the present study are also shown.

Group (Figs. 3a and b). Numerous mafic–ultramafic complexes are distributed along the Damiao-Hongshila Fault (Zhang et al., 2009). Based on zircon U-Pb dating, the emplacement ages of these complexes are considered to fall within the Late Paleozoic to Early Mesozoic (Zhang et al., 2009). However, the Liuying complex, notable for its substantial size among these formations, lack reliable age data.

The Liuying I complex is irregularly shaped, extending approximately 6 km in length and 1 km in width, and is emplaced within the Hongqiyingzi Group (Fig. 2b). Complexes II and III, each with dimensions of < 2 km in length and < 0.5 km in width, are located approximately 1–2 km away from Complex I. They are also emplaced in the Hongqiyingzi Group. These three complexes are predominantly composed of hornblendite and plagioclase hornblendite, which appear relatively fresh and exhibit weak deformed and metamorphosed.

The hornblendite exhibits dark green color and cumulate texture (Figs. 3c and d). The mineral assemblages are composed of amphibole (>98 vol%) and plagioclase (<2 vol%). The amphibole is euhedral and granular with size of 0.5–7 mm. Single twins and poikilitic texture are commonly present (Fig. 3c), suggesting magmatic crystallization (Triantafyllou et al., 2018). The plagioclase hornblendite is also composed of amphibole (90–95 vol%) and plagioclase (5–10 vol%), with cumulate texture (Figs. 3e and f). The plagioclase is subhedral and grows within euhedral amphibole as intergranular phase.

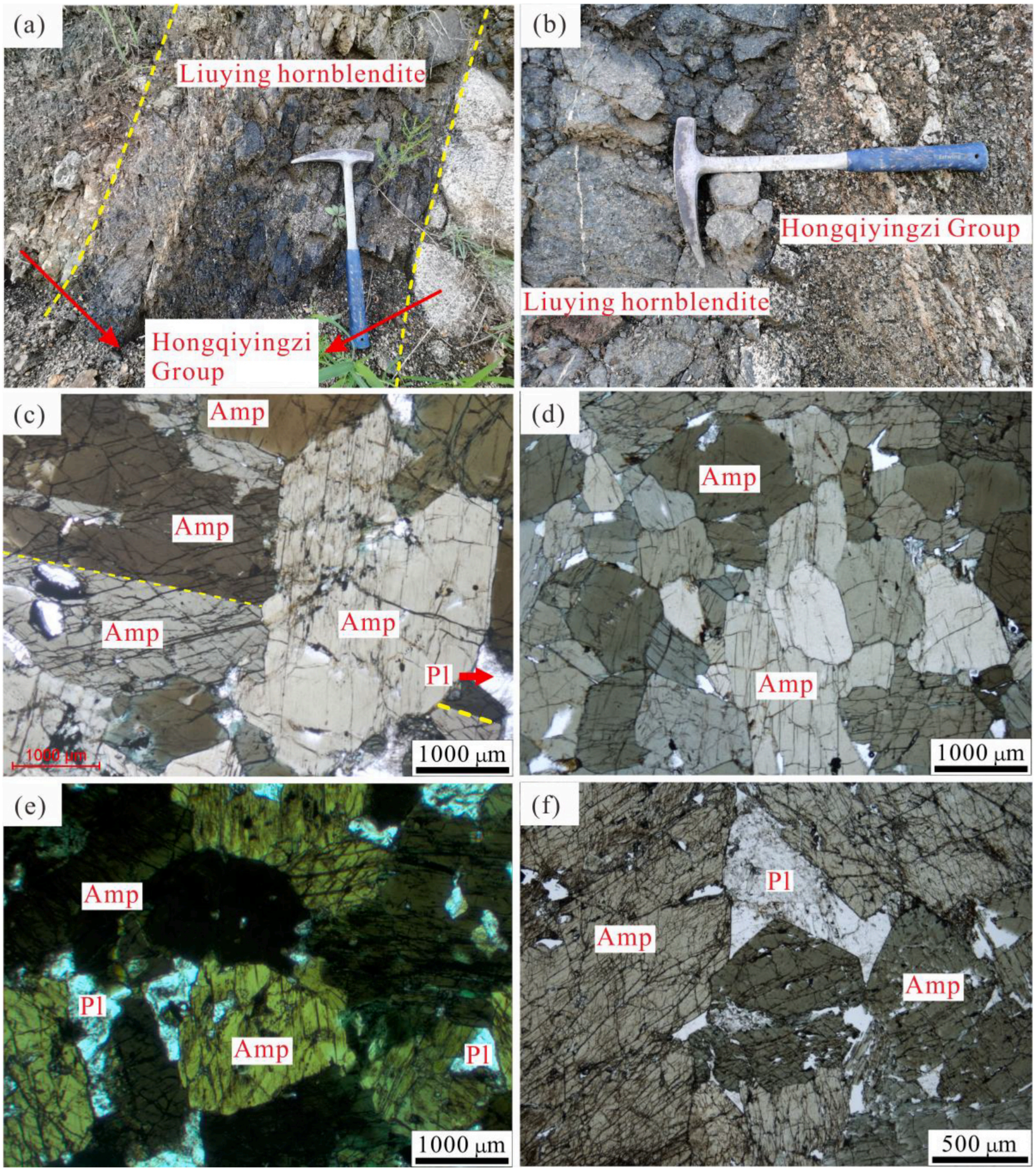

Fig. 3. Representative field photographs (a-b) and section microphotographs (c-f) of the Liuying ultramafic complex: (a) the complex intruded into Archean-Paleoproterozoic Hongqiyingzi Group plagioclase amphibolite; (b) Magmatic intruded connection between the ultramafic complex and amphibolite; (c) Hornblendite, amphibole shows single twins and poikilitic texture; (d) Hornblendite with cumulated texture; (e) Plagioclase hornblendite with cumulate texture, the amphibole is euhedral and intergranular plagioclase is subhedral; (f) Plagioclase hornblendite with euhedral amphibole; Abbreviations: Amp, amphibole; Pl, plagioclase.

4. Analytical methods

Fresh hornblendite (19LY-1-3) and plagioclase hornblendite (21LY-3-1) samples from the Liuying I complex were selected for zircon separation U-Pb dating and Lu-Hf isotope analysis. A total of nineteen fresh samples, comprising ten hornblendites and nine plagioclase hornblendites, were selected for whole-rock geochemistry, mineral geochemistry, Sr-Nd isotope, and amphibole Sr isotope analysis.

More than 10 kg from each sample were selected for the separation of zircon. Zircon grains were separated using conventional heavy liquid and magnetic separation techniques. The zircon grains were then mounted in epoxy and polished. Transmitted and reflected light microscopy, combined with cathodoluminescence (CL) imaging, was employed to select laser ablation targets. Detailed analytical methods can be found in Liu et al. (2024). Zircon U-Pb geochronology and trace element analyses were performed using an excimer (193 nm wavelength) LA-ICP-MS at the State Key Laboratory of Geological Processes and Mineral Resources (GPMR), China University of Geosciences (CUG), Wuhan. The instrument integrates a quadrupole Thermo Fisher iCAP RQ ICP-MS, equipped with a GeoLasPro laser-ablation system. During the LA-ICP-MS analyses, the laser energy density, ablation frequency, and laser spot diameter were set to be 4 J/cm^2, 8 Hz and 32 μm. The glass NIST 612 and ^{29}Si were used as external and internal standards, respectively, to calibrate the zircon analyses. Harvard zircon 91,500 (1065.4 ± 0.3 Ma, Wiedenbeck et al., 2004) was utilized to assess U-Pb isotope fractionation effects. Concordia ages and diagrams were generated using Isoplot 4.11 software (Ludwig, 2003).

Whole-rock major elemental compositions were determined using X-ray fluorescence spectrometry (XRF) with a Shimadzu Sequential 1800 spectrometer at the GPMR, CUG, Wuhan. The sample powder (0.7 g) was mixed with 6 g of compound flux ($Li_2B_4O_7$: $LiBO_2$ = 12:22) and melted into glass sheets in a high-frequency melting furnace at 1000 °C for 15 min. The analytical conditions included a duration of 30–60 s, with a current of 70 mA and a voltage of 40 kV. Repeated samples (one in six samples) and the Chinese National standard GBW07123 were selected to monitor the analyses and data quality. Based on the analytical values of the standards, the errors for major elements are less than 5 % relative.

Whole-rock trace elemental contents were analyzed using an Agilent 7700e ICP-MS with a shielded torch at the Wuhan Sample Solution Analytical Technology Co., Ltd. The sample powder (50 g) was mixed with 1 ml of HNO_3 and 1 ml of HF in a Teflon bomb at 190 °C for over 24 h, followed by evaporation to dryness. HNO_3 (1 ml), MQ water (1 ml), and a 1 ppm internal standard solution (1 ml) were placed in a Teflon bomb, which was then sealed and placed in an oven at 190 °C for over 12 h. Three standards (BHVO-2, BCR-2 and RGM-2) were employed to monitor the quality of the analytical values. Errors for trace-element analyses were estimated to be within 5 % based on reference materials.

Four hornblendites (eight thin sections) and eight plagioclase hornblendites (ten thin sections) were selected for the mineral analyses. Major elemental compositions of minerals were determined on carbon-coated polished sections using a JEOL JXA-8100 Electron Probe Micro Analyzer (EPMA) at the GPMR, CUG, Wuhan. The EPMA was equipped with four wavelength-dispersive spectrometers and operated at an acceleration voltage of 15 kV, a beam intensity of 20 nA, and a spot diameter of 5 μm. Analytical data were matrix-corrected using the ZAF (atomic number, absorption and fluorescence) correction procedure. LA-ICP-MS mineral trace elemental analyses were conducted using a laser denudation system equipped with a RESOlution S155 193 nm ArF excimer laser at GPMR, CUG, Wuhan. The ICP-MS used was a Thermo Fisher iCAP RQ. All analyses were conducted at a denudation frequency of 10 Hz, an energy density of 4 J/cm^2, and a spot diameter of 50 μm. NIST SRM 612 and 610, along with USGS (BIR-1G, BCR-2G, BHVO-2G) reference standard samples, were analyzed alternately for every 6 to 8 unknown samples.

Whole-rock Sr-Nd isotopic compositions were determined using a Neptune XT MC-ICP-MS at Nanjing Hongchuang Exploration Technology Service Co., Ltd, Nanjing. The ^{87}Rb/^{86}Sr and ^{147}Sm/^{144}Nd ratios were calculated based on measured whole-rock Rb, Sr, Sm, and Nd concentrations obtained via ICP-MS. The ^{143}Nd/^{144}Nd were corrected for mass fractionation, normalizing to ^{146}Nd/^{144}Nd = 0.7219, and the ^{87}Sr/^{86}Sr ratios were normalized to ^{86}Sr/^{88}Sr = 0.1194. During the analysis periods, the measured values for the RGM-2 and JB-3 Sr-Nd standards were ^{87}Sr/^{86}Sr = 0.704155 ± 0.000007 (2σ), ^{143}Nd/^{144}Nd = 0.512806 ± 0.000007 (2σ), and^{7}Sr/^{86}Sr = 0.703428 ± 0.000008 (2σ), ^{143}Nd/^{144}Nd = 0.513069 ± 0.000008.

Zircon Hf isotopic analyses were performed using a Nu Plasma II MC-ICP-MS, coupled with a 193 nm RESOlution S-155 laser-ablation system at GPMR, CUG, Wuhan. All analyses were performed directly over the same pits used for U-Pb age dating, employing a laser energy of 4.5 J/cm^2, an ablation frequency of 10 Hz, and a spot diameter of 50 μm. The measured ^{176}Hf/^{177}Hf values of the Zircon Penglai standards yield an average value of 0.282891 ± 0.000020 (2σ) in this study, which is consistent with the reference value of 0.282906 ± 0.000010 (Li et al., 2010).

Sr isotope analysis of amphibole was selected from variable grain sizes of five hornblendite samples and five plagioclase hornblendite samples. The laser ablation system used in the experiments was manufactured by RESOlution, model RESOlution-S155, and the multi-collector inductively coupled plasma mass spectrometer was made by Nu Instruments, model Nu Plasma II. The laser energy for Sr isotope analysis was set at 3 J/cm^2, with an ablation spot diameter of 75 to 130 μm, an ablation frequency of 12 Hz, and an ablation time of 40 s. The reference materials used in this analysis were internal standards from the laboratory, including modern corals from the Indian Ocean and Qingdao. The ^{87}Sr/^{86}Sr ratios of standards obtained from this analysis was 0.70918 ± 0.00005 (2σ, n = 29), which is consistent with the reported value in the literature (Bizzarro et al., 2003).

5. Analytical results

5.1. Zircon u-pb dating and trace element

The representative zircon CL images and zircon dating results for the hornblendite and plagioclase hornblendite are presented as concordia diagrams in Figs. 4 and 5, respectively, with a detailed dataset provided in Supplementary Material Table S1. The age data histograms with probability curves and chondrite-normalized rare earth elements (REE) pattern diagrams are shown in Fig. 6, with a detailed dataset provided in Table S2. The characteristics of zircon and the age results from individual samples are described below.

5.1.1. Hornblendite

Zircon grains from the hornblendite can be divided into two groups: (1) The subhedral to sub-rounded zircons with fuzzy banded zoning, and most of grains are structureless domains with prominent pale overgrowths; (2) The subhedral to euhedral zircons with clear oscillatory zoning.

The lengths of subhedral to sub-rounded zircons range from 80 to 150 μm, with length-to-width ratios of 1.5:1–1:1. In the CL images, most zircon grains exhibit a typical core-rim texture, characterized by homogeneous core and structureless rim (Fig. 4). These zircons have Th concentrations ranging from 10.6 to 551 ppm and U concentrations from 16.3 to 752 ppm, resulting in Th/U ratios of 0.33–1.03. In the chondrite-normalized REE pattern diagram (Fig. 6c), the zircons display widely left-declining patterns with negative Eu anomalies (δEu = 0.01–0.18), positive Ce anomalies (δCe = 12.3–756), and REE content of 208–1311 ppm. A total of twenty-two spots were analyzed from twenty-two zircon grains, and the age data can be categorized into three groups. Fifteen analyses of zircons have ^{207}Pb/^{206}Pb ages of 1918–1999 Ma, yield a ^{207}Pb/^{206}Pb weighted mean age of 1958 ± 24 Ma, (MSWD = 0.34, n = 15) (Figs. 5a and b). Two analyses of zircons yielded a ^{207}Pb/^{206}U age range of 1798–1791 Ma, while five spots yielded a ^{206}Pb/^{238}U age range

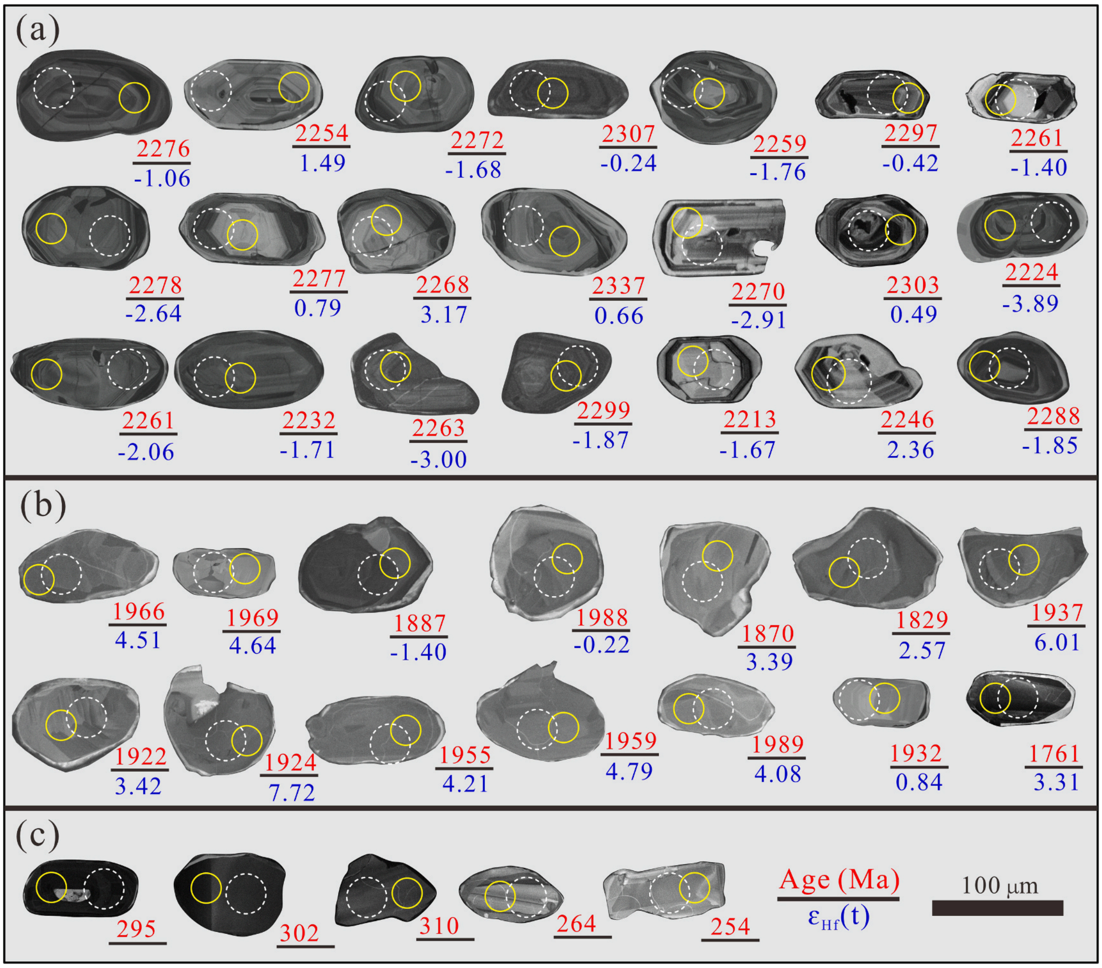

Fig. 4. Representative zircon cathodoluminescence images for the Liuying ultramafic complex from the northern North China Craton: (a) Zircons with $^{207}Pb/^{206}Pb$ ages of 2213–2337 Ma and $\varepsilon_{Hf}(t)$ −3.89 to + 3.17 show clear oscillatory zoning; (b) Zircons with $^{207}Pb/^{206}Pb$ ages of 1761–1989 Ma and $\varepsilon_{Hf}(t)$ −1.40 to + 6.01 show homogeneous core and structureless rim; (c) Zircons with $^{206}Pb/^{238}U$ ages of 254–310 Ma display fuzzy banded zoning and structureless core. Ages and $\varepsilon_{Hf}(t)$ values are shown in yellow and white circles, respectively.

of 246–310 Ma.

The zircons with oscillatory zoning have lengths ranging from 50 to 150 μm and widths ranging from 50 to 80 μm (Fig. 4). These zircons have Th concentration ranging from 26.7 to 539 ppm and U concentration from 37.8 to 666 ppm, resulting in Th/U ratios of 0.43 to 3.16 (Table S1), indicating a magmatic origin (Griffin et al., 2002). Seventeen analyses of zircons yielded a $^{207}Pb/^{206}Pb$ weighted mean age of 2274 ± 39 Ma, (MSWD = 0.16, n = 17) (Fig. 5d). These zircons display similar left-declining patterns (Fig. 6c), with negative Eu anomalies (δEu = 0.02–0.71), positive Ce anomalies (δCe = 26.9–745), and high REE content (143–2823 ppm).

5.1.2. Plagioclase hornblendite

Zircon grains from the plagioclase hornblendite (21LY-3-1) can also be categorized into two groups, which exhibit characteristics similar to those of zircons from hornblendite (Fig. 5e–h).

The zircons with core-rim texture have Th of 13.9–467 ppm and U of 54.4–400 ppm with Th/U ratios of 0.14–1.17 (Table S1). In the chondrite-normalized REE pattern diagram (Fig. 6d), the zircons display widely left-declining patterns with negative Eu anomalies (δEu = 0.04–0.25), positive Ce anomalies (δCe = 5.09–468), and REE content of 38.0–1652 ppm. A total of fifteen spots were analyzed from fifteen zircon grains, and the data can be categorized three groups. Eleven analyses of zircons have $^{207}Pb/^{206}Pb$ ages of 1955–1829 Ma, yielded a $^{207}Pb/^{206}Pb$ weighted mean age of 1892 ± 23 Ma (MSWD = 0.75, n = 11) (Fig. 5f). Three analyses of zircons yielded a $^{206}Pb/^{238}U$ age of 302–262 Ma. One zircon has a $^{207}Pb/^{206}U$ age of 1761 Ma.

The second group of zircons exhibiting oscillatory zoning has Th concentrations ranging from 17.2 to 516 ppm and U concentrations from 23.3 to 1051 ppm, resulting in Th/U ratios of 0.46–1.73 (Table S1), which also indicate a magmatic origin. In the chondrite-normalized REE pattern diagram (Fig. 6d), the zircons display widely left-declining patterns with negative Eu anomalies (δEu = 0.05–0.24), and positive Ce anomalies (δCe = 25.1–1096). Fifteen analyses of zircons yielded a $^{207}Pb/^{206}Pb$ weighted mean age of 2257 ± 38 Ma, (MSWD = 0.15, n = 15) (Fig. 5h).

5.2. Whole-rock major and trace elements

The whole-rock major and trace element compositions are provided in Table S3. The major and trace element chemistry of the Liuying ultramafic rocks is controlled by the modal proportions of amphibole and plagioclase. The hornblendite exhibit $Mg^{\#}$ values ranging from 0.68 to 0.76 (MgO = 12.6–15.7 wt%), SiO_2 contents from 41.9 to 46.1 wt%, Al_2O_3 contents from 10.0 to 15.5 wt%, TiO_2 contents from 1.24 to 1.91 wt%, FeO_{tot} contents from 10.0 to 13.6 wt%, CaO contents from 10.1 to 12.2 wt%, and Na_2O contents from 1.48 to 2.56 wt%. As the modal proportions of plagioclase increase, SiO_2 and Al_2O_3 contents increase with decreasing MgO and FeO_{tot}, whereas CaO contents remain almost unchanged (Fig. 7). The plagioclase hornblendite has SiO_2 of 41.2–48.1

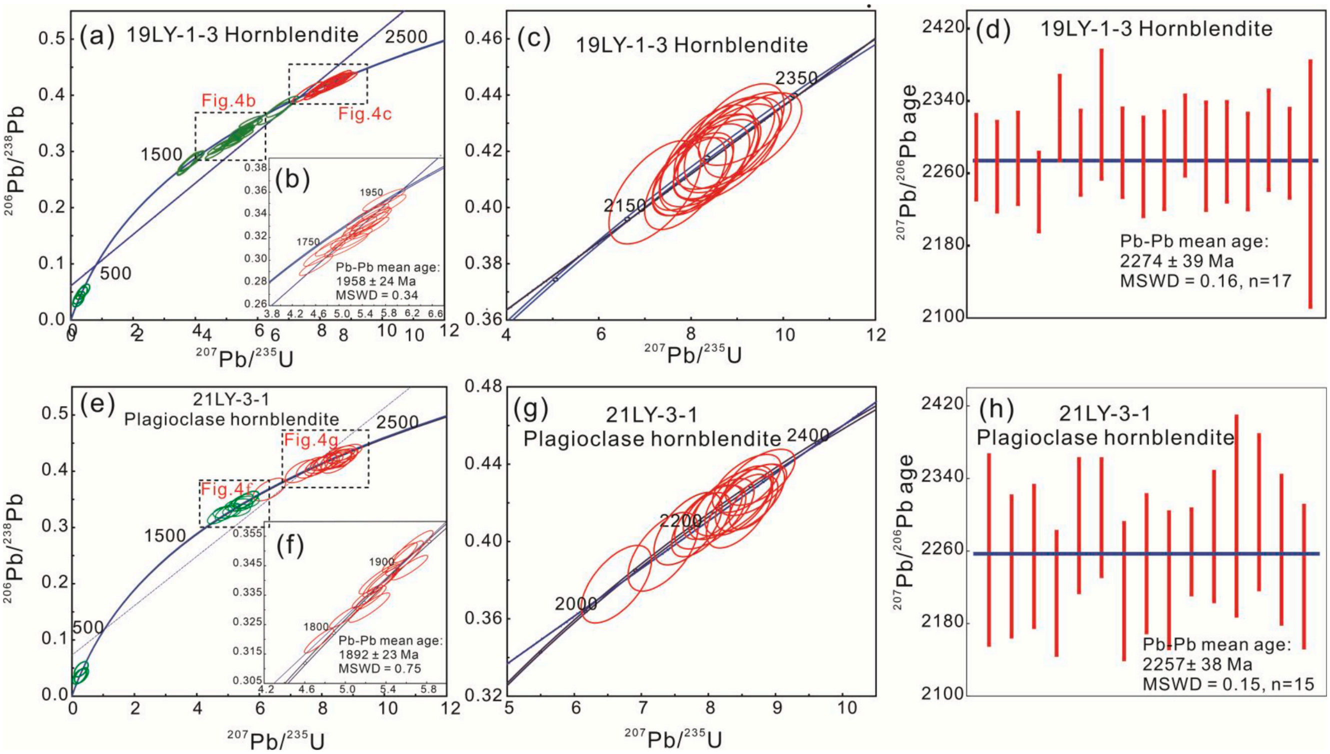

Fig. 5. (a-c) zircon U-Pb concord diagram and (d) weighted mean ^{207}Pb/^{206}Pb ages for the Liuying hornblendite; (e-g) Zircon U-Pb concord diagram and (h) weighted mean ^{207}Pb/^{206}Pb ages for the Liuying plagioclase hornblendite.

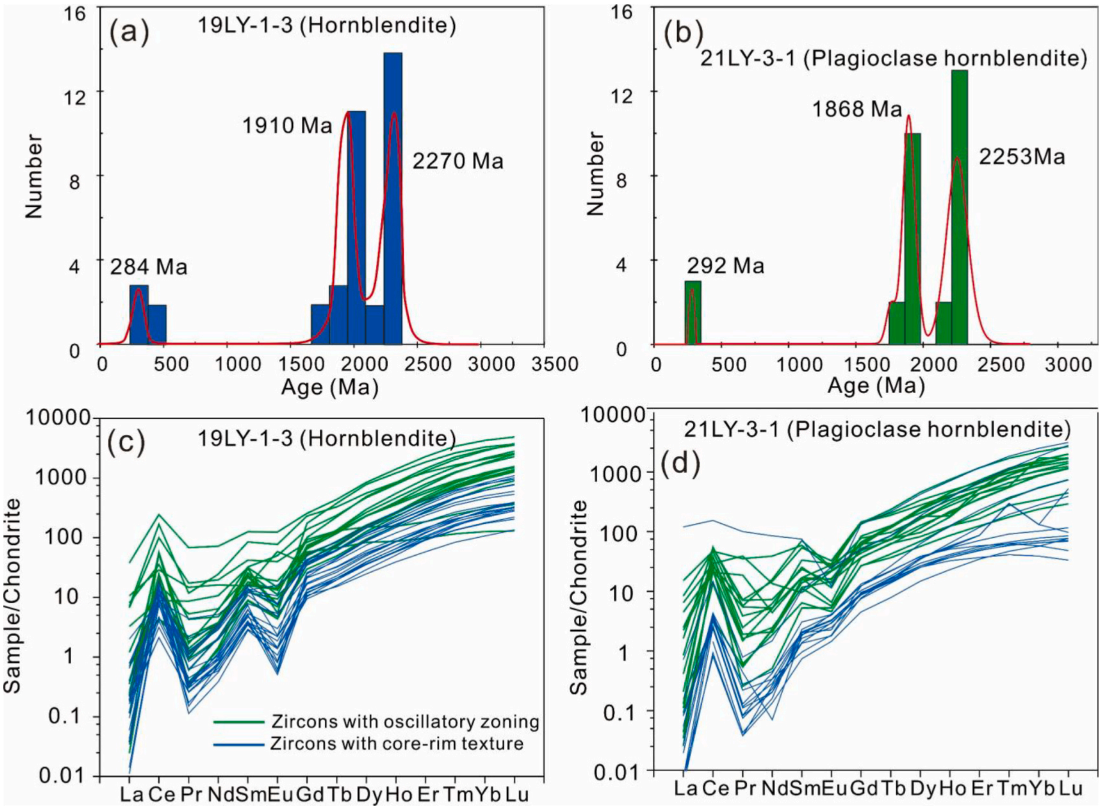

Fig. 6. (a-b) The age data histograms with probability curves and (c-d) Chondrite-normalized REE patterns for the Liuying ultramafic igneous rocks from northern North China Craton. The normalization values are taken from McDonough et al. (1995).

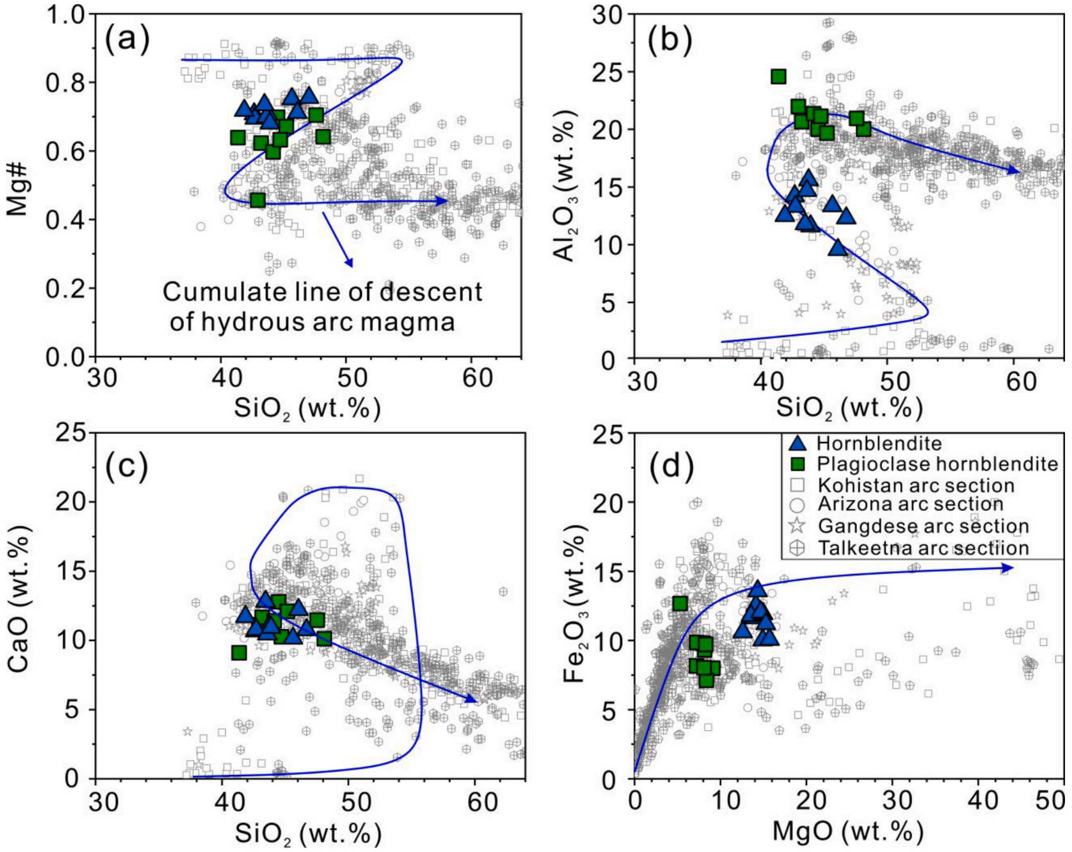

Fig. 7. Harker diagrams illustrating the different fractionation trends for the Liuying ultramafic complex. The blue solid lines refer to the trajectories of cumulate evolution for hydrous fractionation experiments (Müntener and Ulmer, 2018). (a) SiO_2 versus $Mg^{\#}$ values; (b) SiO_2 versus CaO; (c) SiO_2 versus Al_2O_3; (d) MgO versus Fe_2O_3. The data of the Kohistan arc sections are from Jagoutz et al. (2006, 2011); The data of the Arizona arc sections are from Chen et al. (2020); The data of the Gangdese arc sections are from Guo et al. (2020), and the data of the Talkeetna arc sections are from Kelemen et al. (2003), Greene et al. (2006), Rioux et al. (2007, 2010), Hacker et al. (2008).

wt%, Al_2O_3 of 19.9–23.1 wt%, MgO of 5.30–11.3 wt% and FeO_{tot} of 7.12–12.7 wt%.

In the chondrite-normalized REE pattern diagram (Fig. 8a), ultramafic rocks exhibit similar slight light REE (LREE) enrichment with slight right-declining patterns (La_N/Yb_N = 1.20–2.38), and strong enrichment in middle REE (MREE) enrichment (Nd_N/Yb_N = 2.38–4.45). These samples have weakly negative to slightly positive Eu anomalies ranging from 0.88 to 1.26. As illustrated in the primitive mantle-normalized trace element diagram (Fig. 8b), rocks are enriched in LILEs (e.g., LREE, Rb, Ba, Sr), and depleted in HFSEs (Nb, Ta, Zr, Hf).

5.3. Mineral geochemistry

5.3.1. Amphibole

The compositions of amphibole are provided in Table S4. The amphibole in the Liuying ultramafic complex is classified as pargasite

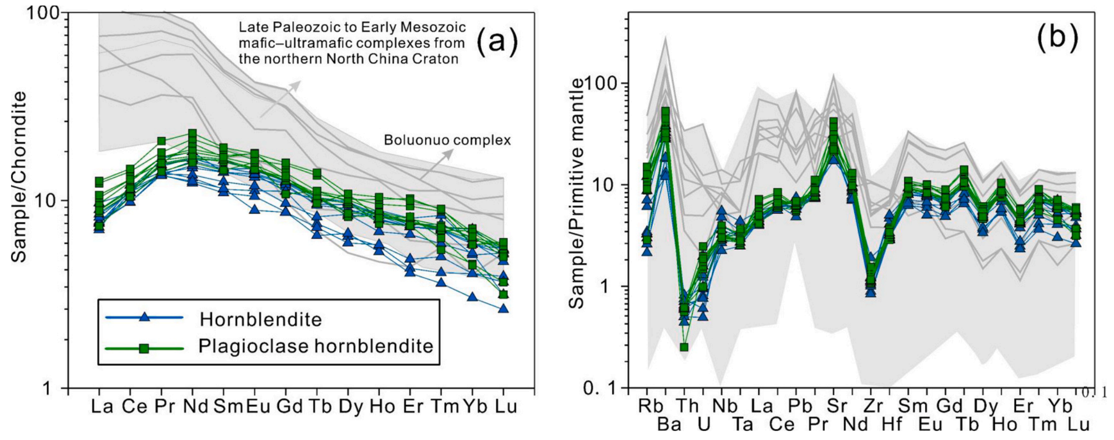

Fig. 8. (a) Chondrite-normalized REE patterns and (b) primitive-mantle-normalized trace-element patterns for the Liuying ultramafic complex. The normalization values for chondrite and primitive mantle are taken from McDonough et al. (1995). The data of the Late Paleozoic to Early Mesozoic mafic–ultramafic complexes from the northern North China Craton are from Zhang et al. (2009), Ma et al. (2013), Liu et al. (2024).

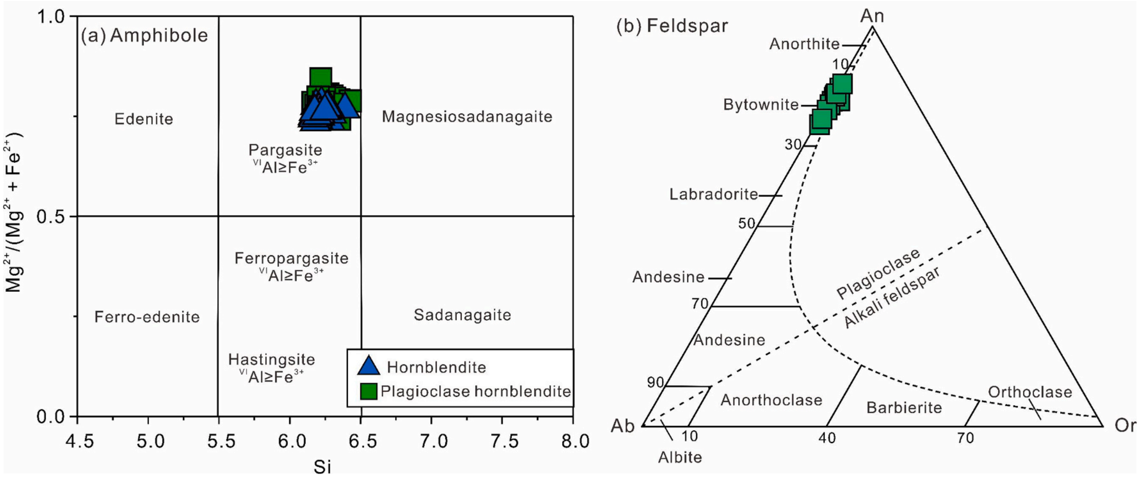

Fig. 9. Compositional diagrams showing the chemistry of representative minerals in the Liuying complex; (a) Classification diagram of amphibole (Leake et al., 1997); (b) Classification of plagioclase (Dai et al., 2021).

(Fig. 9a) (Leake, 1997) and exhibit similar major element compositions (MgO = 13.4–14.9 wt%, FeO_{tot} (Fe_2O_3 and FeO total) = 9.51–11.3 wt%, TiO_2 = 1.35–2.16 wt%, Al_2O_3 = 12.9–14.2 wt%). The amphibole exhibits significant enrichment in MREE and depletion in HREE (La_N/Yb_N = 0.78–4.00, Nd_N/Yb_N = 2.30–6.98), with weak Eu anomalies (δEu = 0.81–1.39) (Fig. 10a). The amphibole is enriched in LILEs, depleted in HFSEs, and exhibits clear negative anomalies of Th, U, Pb, Zr, and Hf, as well as positive anomalies of Ti and K (Fig. 10b).

Amphiboles in plagioclase hornblendite exhibit statistically significant compositional differences compared to those in hornblendite. Specifically, they contain lower Cr (1.63–56.2 ppm) and Ni (9.84–56.6 ppm) concentrations but higher total REE contents (ΣREE = 42.5–84.5 ppm). In contrast, amphiboles in hornblendite show elevated Cr (73.9–1680 ppm) and Ni (111–239 ppm) with reduced ΣREE abundances (30.0–41.1 ppm).

5.3.2. Plagioclase

The compositions of plagioclase are provided in Table S5. Plagioclase is predominately present in the plagioclase hornblendite. It typically exhibits relatively uniform oxide compositions (SiO_2 = 47.3–48.5 wt%,

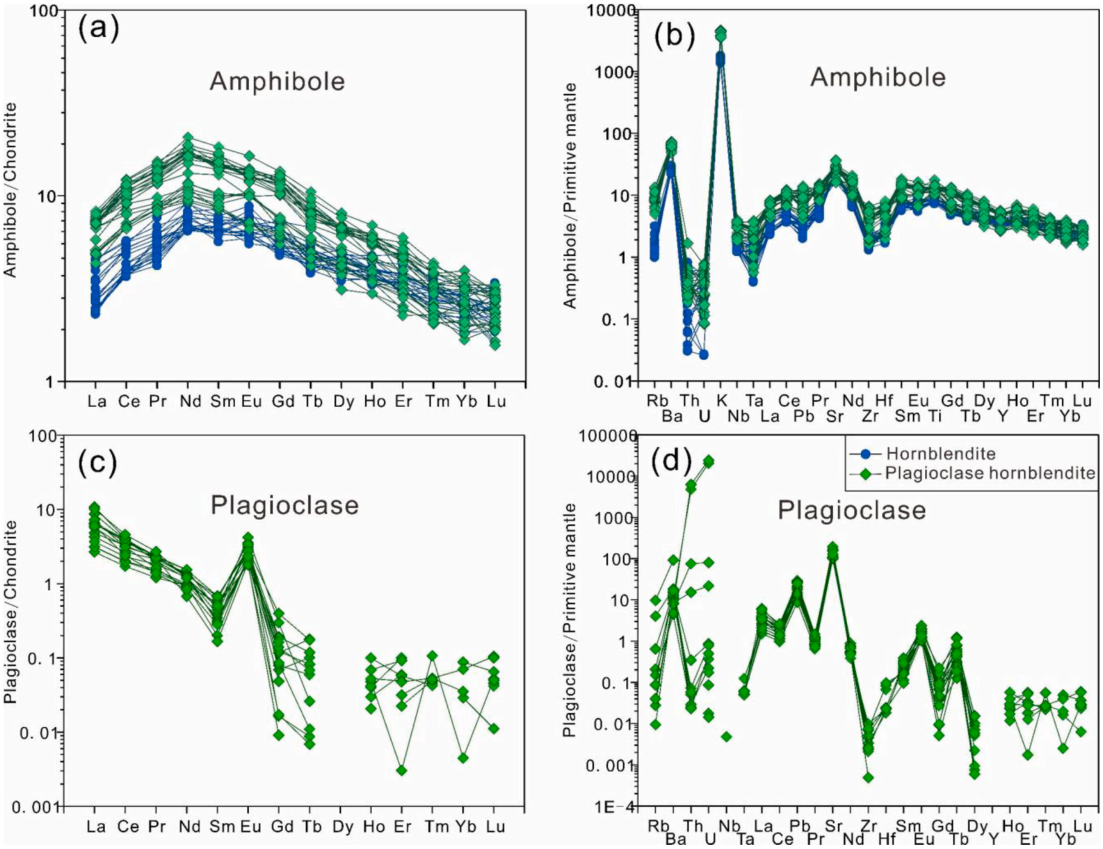

Fig. 10. Chondrite-normalized REE patterns (a and b), primitive-mantle-normalized trace-element patterns (c and d) for the amphibole and plagioclase of the Liuying ultramafic complex. The normalization values for chondrite and primitive mantle are the same as those in Fig. 7.

Al_2O_3 = 32.6–33.8 wt%, CaO = 15.1–17.1 wt%, Na_2O = 1.44–2.89 wt%) and rang from anorthite to bytownite (An = 74–86 %, Ab = 0.14–0.26 %, Or = 0.00–0.02 %) (Fig. 9b). Plagioclase exhibits limited variation in trace element abundances (e.g., $\sum$REE = 3.89–9.64 ppm) and is enriched in LREE, with positive anomalies of Eu (δEu = 5.46–28.8) (Fig. 10c). In the multi-element primitive mantle–normalized diagram (Fig. 10d), plagioclase is characterized by enrichments in LILEs with notable peaks at Pb and Sr.

5.4. Sr-Nd-Hf isotopes

Whole-rock Sr-Nd isotopic compositions are provided in Table S6. The $(^{87}Sr/^{86}Sr)_i$ ratios and $\varepsilon_{Nd}(t)$ values of the hornblendite and plagioclase hornblendite are calculated for ages of 2274 Ma and 2257 Ma, respectively. The hornblendite and plagioclase hornblendite exhibit overlapping $(^{87}Sr/^{86}Sr)_i$ values (initial $^{87}Sr/^{86}Sr$) ranging from 0.704185 to 0.705932 and negative $\varepsilon_{Nd}(t)$ values from −14.6 to −5.68 (Fig. 11a). The $^{87}Sr/^{86}Sr$ ratios of amphibole from hornblendite and plagioclase hornblendite also show overlapping values of 0.705110–0.705846 (Table S7), which is similar to those values of the rocks (0.704616–0.706987) (Fig. 11b).

Zircons Lu-Hf isotopic compositions are provided in Table S8. For the hornblendite, zircons with ages of 2211–2343 Ma exhibit $\varepsilon_{Hf}(t)$ values ranging from −5.96 to + 3.17, with $(^{176}Hf/^{177}Hf)_i$ ratios varying from 0.281163 to 0.281427 and Hf-depleted model ages (T_{DM}) ranging from 2.85 to 2.52 Ga (Fig. 11c). Zircons with ages of 1922–2083 Ma exhibit $\varepsilon_{Hf}(t)$ values ranging from −0.22 to + 9.05, with $(^{176}Hf/^{177}Hf)_i$ ratios varying from 0.281512 to 0.281776 and Hf-depleted model ages (T_{DM}) ranging from 2.02 to 2.39 Ga. The zircons of plagioclase hornblendite with ages of 2211–2343 Ma have $\varepsilon_{Hf}(t)$ values of −3.04 to + 2.36, with $(^{176}Hf/^{177}Hf)_i$ ratios varying from 0.281261 to 0.281418 and Hf-depleted model ages (T_{DM}) ranging from 2.50 to 2.71 Ga. Zircons with ages of 1829–1955 Ma has $\varepsilon_{Hf}(t)$ values of −1.10 to + 4.21, with $(^{176}Hf/^{177}Hf)_i$ ratios varying from 0.281543 to 0.281757 and Hf-depleted model ages (T_{DM}) ranging from 2.04 to 2.33 Ga).

6. Discussion

6.1. Age of the Liuying ultramafic complex

Reports of zircon occurrences in mafic–ultramafic plutons are largely limited to early-stage rocks prior to the crystallization of amphibole (Grimes et al., 2009). However, some reports support the growth of magmatic zircon in hornblendite (Teng et al., 2015; Guo et al., 2020; Zhu et al., 2022, 2024; Liu et al., 2024). Itano et al. (2024) substantiate two conceptual crystallization mechanisms: Crystallization at the mineral-melt interface during the early stages and crystallization from the last drop of interstitial melt during the final stages. During the late stage, the compositional change of trapped melts from mafic to felsic results in zircon saturation due to reduced zircon solubility (Crisp et al., 2023), which could explain the crystallization of magmatic zircons in hornblendite. The calculated melt compositions in equilibrium with the Liuying ultramafic cumulates have SiO_2 contents of 57.1–61.7 wt% and Al_2O_3 contents of 18.0–18.4 wt% (Table S9), supporting the notion that zircon precipitated from the interstitial felsic melt coexisting with amphiboles.

Numerous mafic–ultramafic complexes in the studied region formed during the Late Paleozoic to Early Mesozoic (Zhang et al., 2009). Although no zircons were separated from the Liuying complex, Zhang et al. (2009) demonstrated that its field occurrence, petrology, mineral

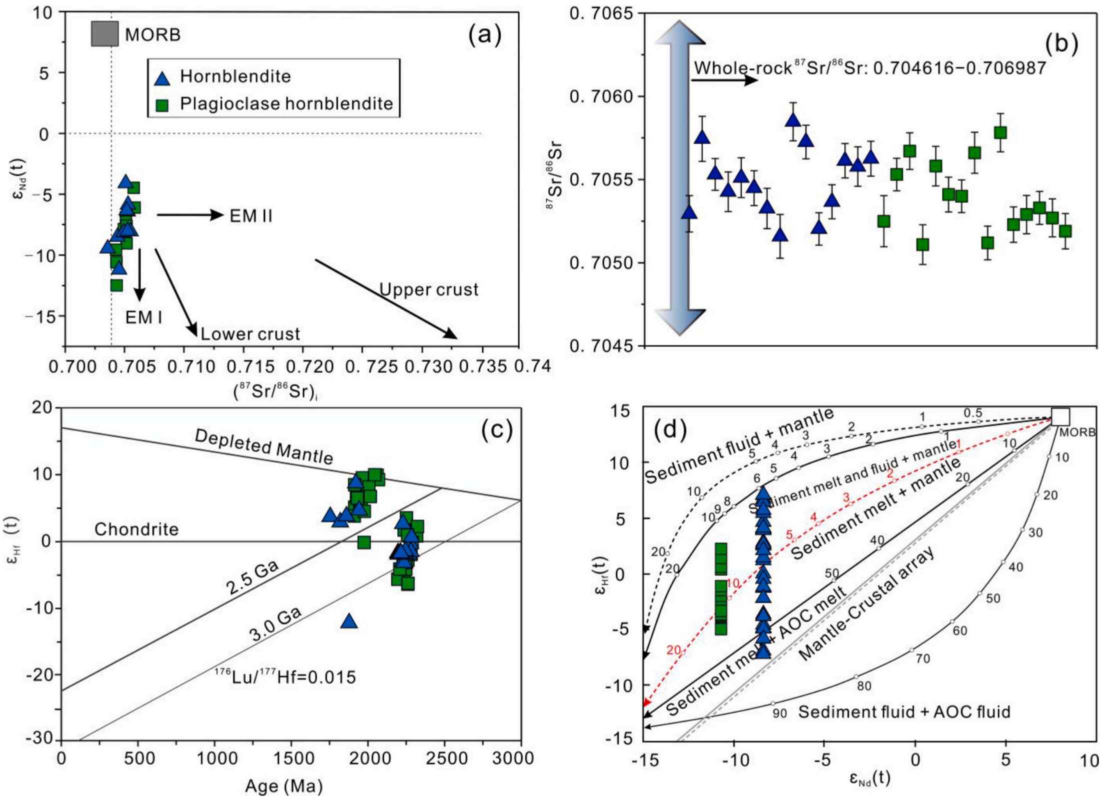

Fig. 11. (a) Whole-rock Sr-Nd isotope, (b) Sr isotopes of amphibole, (c) $\varepsilon_{Hf}(t)$ versus U–Pb age of zircons, and (d) whole-rock $\varepsilon_{Nd}(t)$ versus zircons $\varepsilon_{Hf}(t)$ discriminant diagrams for the Liuying ultramaficcomplex. Mantle wedge data ε_{Nd} = +8, Nd = 1.7 ppm, $(^{87}Sr/^{86}Sr)_i$ = 0.703, Sr = 25 ppm; The red dashed line corresponds to the mixing between the mantle wedge and mixed sediment melt (ε_{Hf} = –13.7, ε_{Nd} = –15.5). Trace element concentrations of the mixing members are from Hanyu et al. (2006). The trace elements and Sr-Nd isotope compositions for mantle wedge peridotite are from Salters and Stracke (2004), Gale et al. (2013); and the sediment are represented by GLOSS-jj (Plank, 2014).

assemblages, and geochemical/isotopic compositions closely resemble those of the Boluonuo complex. However, the following lines of evidence, including zircon U-Pb ages, textures, compositions, and geothermometry, along with lithology, mineral assemblages, geochemical signatures, and isotopic systematics, collectively preclude a Late Paleozoic formation age for the studied rocks, indicating instead a Paleoproterozoic origin.

The zircon grains analyzed in this study exhibit three distinct age populations of 2211–2343 Ma, 1761–1999 Ma, and 246–310 Ma (Figs. 4 and 6). The zircon with age population of 2211–2343 Ma have clear oscillatory zoning and high Th/U ratios (0.43–3.16 with an average value of 1.10), suggesting their magmatic origin (Griffin et al., 2002). Furthermore, the weighted mean ^{207}Pb/^{206}Pb age of the ultramafic rocks is younger than those of the wall rocks (2546–2532 Ma, Hongqiyingzi Group quartz dioritic-tonalitic-granodioritic gneisses) (Liu et al., 2019), which is consistent with field observation. The presence of euhedral, oscillatory-zoned zircons in mafic rocks may reflect origins unrelated to contemporaneous crystallization. For instance, zircon xenocrysts from the Cenozoic Caiyuanzi basalts (Liaodong Peninsula, North China Craton) are euhedral and show clear oscillatory zoning. They yield U-Pb ages ranging from ~ 100 Ma to 2570 Ma (Zhang et al., 2011). In contrast, oscillatory-zoned zircons from the Liuying complex display a narrow age distribution, yielding concordant ^{207}Pb/^{206}Pb weighted mean ages of 2274 ± 39 Ma (MSWD = 0.16, n = 17) and 2257 ± 38 Ma (MSWD = 0.15, n = 15) (Figs. 4 and 5). Moreover, Paleozoic zircons observed in this study are scarce, morphologically heterogeneous, and cover an extensive age range, showing characteristics inconsistent with magmatic zircon origins. Consequently, the weighted mean ^{207}Pb/^{206}Pb ages of 2257–2274 M a is considered to represent the crystallization age of the Liuying ultramafic complex. Our new data are comparable to those reported for ultramafic–mafic igneous rocks within or adjacent to the northern NCC (Kusky et al., 2016, Zhang et al., 2023), indicating that the northern NCC experienced intense Early Paleoproterozoic magmatism.

The zircons with age populations of 1761–1999 Ma and 246–310 Ma display lower Th/U ratios of 0.14–1.17, subhedral shape and fuzzy zoning texture, suggesting their metamorphic origin (Fig. 4). It might origin from dissolution-reprecipitation processes (Hoskin and Schaltegger, 2003). At ca. 2.0–1.8 Ga, the North China Craton underwent extensive subduction and collisional orogeny, coupled with mantle upwelling as well as diabase magmatism, resulted in widespread crustal thermal events and high-pressure granulite facies metamorphism (Zhao et al., 2005). These events are likely recorded by metamorphic zircons from the Liuying ultramafic complex, as well as metamorphic detrital zircon with a peak crystallization age of ~ 1897 Ma within the northern NCC (Fig. 12). Additionally, metamorphic zircons with ages of 262–354 Ma are also present in the ultramafic complex, which likely resulted from Phanerozoic multiple tectono-magmatic events within the northern NCC (Zhang et al., 2007, Zhang et al., 2009).

Furthermore, Ti-in-zircon thermometry calculations (Watson and Harrison, 2005) reveal that magmatic zircons with ages of 2211–2343 M a record temperatures ranging from 662 to 1045°C, higher than 679–904°C recorded by metamorphic zircons (246–1999 M a). Therefore, the zircon U-Pb ages of 246–1999 Ma mentioned above may record the ages of later thermal overprinting and should not be interpreted as the formation ages of studied ultramafic rocks. Most metamorphic zircon thermometry constrains temperatures to ~ 700 °C, consistent with amphibolite-facies conditions. The Liuying complex (emplaced at mid- to lower-crustal depths) exhibits an amphibole-dominant assemblage (>90 vol%) with subordinate plagioclase (<10 vol%). This metamorphic event involved: (i) Recrystallization of primary amphibole into coarser-grained crystals exhibiting crystalloblastic texture, and (ii) compositional homogenization of amphibole. Amphiboles in the Liuying complex reach lengths of 7 mm, with statistically insignificant compositional variations between hornblendite and plagioclase hornblendite. These features suggest that amphibolite-facies overprinting in the Liuying complex was substantially weaker.

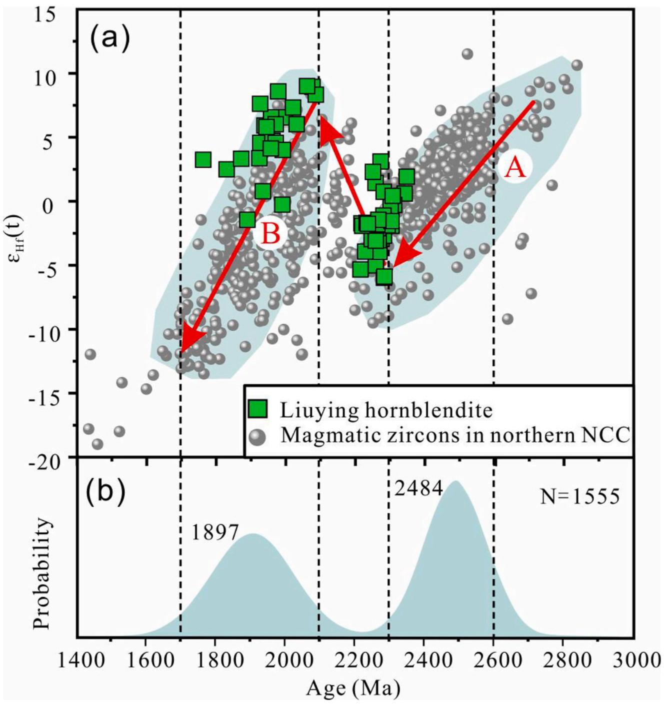

Fig. 12. (a) Normalized relative probability plots of the Liuying magmatic zircons and (b) detrital zircon U-Pb ages of samples from the northern north China Craton. The detrital zircon crystallization ages and Lu-Hf isotope concentrations were from Zhang et al. (2023) and this study.

Field occurrences further distinguish these units: The Liuying complex comprises variably sized lenticular bodies of amphibole + plagioclase. Differently, Late Paleozoic to Early Mesozoic mafic–ultramafic complexes in the studied region intruded as annular/sub-annular stocks composed of peridotite, pyroxenite, hornblendite, and diorite (Liu et al., 2024). Unlike these Phanerozoic units with ubiquitous apatite and magnetite, both minerals are conspicuously absent in the Liuying complex. Trace element compositions (Fig. 8) show significantly lower REE contents and greater depletion in Th, U, and LREE in the Liuying complex relative to Late Paleozoic–Early Mesozoic complexes in the studied region (e.g., Boluonuo complex). Isotopically, Late Paleozoic–Early Mesozoic complexes (e.g., Boluonuo) exhibit enriched signatures: $\varepsilon_{Hf}(t)$ = –17 to –5, $(^{87}Sr/^{86}Sr)_i = 0.70521–0.70604$, and $\varepsilon_{Nd}(t)$ values of ca.–10 (Zhang et al., 2009; Ma et al., 2013; Liu et al., 2024). Conversely, Liuying zircons yield variable $\varepsilon_{Hf}(t)$ values (−6 to + 7). Although Sr-Nd isotopic compositions overlap regionally, this similarity likely reflects heterogeneous source melting rather than coeval magmatism.

6.2. *Effects of shallow-level open-system processes*

Our samples are fresh, showing no signs of alteration, such as carbonation, red oxidation (e.g., hematite and maghemite), or other forms of secondary mineralization upon examination of thin sections. Although the rocks display variable loss on ignition (LOI) values ranging from 1.04 to 2.49 wt%, these values generally do not correlate with the abundances of fluid-mobile elements such as Ba, Pb, U and K_2O (Figs. S1a–d). Therefore, these elements are not affected by post-magmatic alteration. The Rb/Sr ratios in igneous rocks increase with magma differentiation, due to Sr is enriched in the early stages of magma, while Rb behaves conversely. With magma differentiation, the concentrations of incompatible Nb and Ta increase, while the increase in Ta is more significant than that of Nb. As a result, the Nb/Ta ratio decreases from the early to the late stages of magma processes. The decreased Rb/Sr accompanied by increased Nb/Ta suggests that the whole-rock compositions of the Liuying ultramafic rocks are controlled by magmatic differentiation processes (Fig. S1e). Furthermore, the LOI values do not significantly correlate with $(^{87}Sr/^{86}Sr)_i$ ratios (Fig. S1f), indicating that alteration did not affect the isotopic compositions of rocks.

The unchanged $(^{87}Sr/^{86}Sr)_i$ ratios and $\varepsilon_{Nd}(t)$ with increasing SiO_2 (Fig. S2), suggesting that crustal contamination seems to play an insignificant role in the petrogenesis of the studied rocks. In addition, the magmatic processes could cause variations in whole-rock concentrations, these processes would not alter Sr-Nd-Hf isotope compositions. Furthermore, certain features, such as the enrichment in LILEs and depletion in HFSEs, should not change due to mineral accumulation or fractionation during the crystallization and differentiation of mafic magmas (e.g., Hanyu et al., 2006; Zhao et al., 2019).

In summary, the effects of shallow-level open-system processes on the compositions of the studied igneous rocks are minimal. These mafic intrusions formed during the early stages of mafic magmatism, providing valuable insights into the composition of their magma sources.

6.3. Petrogenesis

6.3.1. Magma chamber processes

The Liuying ultramafic complex is composed of hornblendite and plagioclase hornblendite. Previous studies have suggested that the amphibole-rich rocks in the lower to middle crust can form either by fractional crystallization or accumulation from mantle-derived magmas, or via melting reactions involving early formed clinopyroxene, olivine, and residual or externally injected melts (Smith, 2014; Zhou et al., 2020). Several lines of evidence suggest that the studied ultramafic rocks formed via fractional crystallization of mafic magmas, specifically through accumulation processes.

The majority of amphiboles in the hornblendite are idiomorphic crystals, showing no obvious replacement reaction structures (Fig. 3). Some amphiboles exhibit single twins and poikilitic texture (Fig. 3c). The major element compositions of rocks are complementary to typical arc accumulation section from the Kohistan arc in Pakistan (Jagoutz et al., 2011, Jagoutz, 2014), the Arizona in USA (Chen et al., 2020), the Gangdese in China (Guo et al., 2020), and the Talkeetna in USA (Kelemen et al., 2003; Greene et al., 2006; Rioux et al., 2007, 2010; Hacker et al., 2008), which exhibit low SiO_2 and high MgO and Fe_2O_3 contents. The major element composition of hornblendite aligns with the evolutionary trend of water-bearing basalt differentiation under 10 kbar conditions in experimental petrology (Müntener and Ulmer, 2018) (Fig. 7d).

Cumulates lines of descent (CLD) from hydrous arc magmas define: (i) A Z-shaped trend in $Mg^{\#}$ vs. SiO_2 (Fig. 7a); (ii) An S-shaped trend in Al_2O_3 vs. SiO_2 (Fig. 7b); and (iii) A anticlockwise loop-like evolution in CaO vs. SiO_2 (Fig. 7c). These CLD trends are independent of starting arc magma compositions. Different primitive arc magmas generate either silica-rich or silica-poor cumulate sequences at arc crustal bases. The CLD comprises three distinct segments: (i) Ultramafic cumulates (dunites, wehrlites, olivine clinopyroxenites) exhibit substantial SiO_2 enrichment at high $Mg^{\#}$ alongside low Al_2O_3; (ii) Intermediate cumulates display decreasing SiO_2 accompanied by sharp $Mg^{\#}$ depletion and pronounced Al_2O_3 enrichment, forming amphibole ± garnet-dominated assemblages (with minor anorthitic plagioclase and oxides); (iii) Mafic cumulates show increasing SiO_2, culminating in gabbroic compositions. The counterclockwise evolution of CaO reflects early clinopyroxene-dominated crystallization (yielding < 20 wt% CaO), followed by amphibole ± garnet saturation, which depletes bulk CaO and SiO_2. Critically, the Liuying hornblendite cumulates plot within Segment 2 of the CLD (Fig. 7), demonstrating their origin via fractional crystallization of hydrous arc magmas. The REE distribution patterns of the amphibole in the hornblendite are consistent with the whole-rock REE distribution patterns (Figs. 8 and 10). The hump-shaped REE patterns suggest they were controlled by crystallization and accumulation of amphibole, as amphibolite is strongly enriched in MREEs. Furthermore, the mafic igneous rocks in this study exhibit varying SiO_2 contents, which negatively correlate with Dy/Yb ratios, further suggesting fraction crystallization processes controlled by amphibole (Fig. 13d).

The crystallization temperature and pressure of the Liuying rocks are estimated to range in 966–996℃ and 477–600 MPa, respectively, corresponding with middle-lower crustal depths (18–23 km) (Ridolfi et al., 2010) (Table. S9). Fractional crystallization of amphibole primarily affects the concentrations of Ti, Nb Ta and MREE, while the accumulation of plagioclase leads to increase in Eu, Sr and LREE contents. The Liuying ultramafic cumulates shows MREE enrichments relative to LREE and HREE ($Nd_N/Yb_N = 2.38$–4.45) (Fig. 8a) and lack significant negative Eu anomalies, suggesting limited accumulation of plagioclase. This may be related to the high content of water in magmas (Müntener et al., 2001). The calculated water content of the melts in equilibrium with amphibole ranges of 7.3–8.1 wt% (Ridolfi et al., 2010), falls into the water content observed in arc magmas. Plagioclase in the Liuying hornblendite forms intergranular phases among between accumulated amphibole crystals, likely crystallized from residual intergranular melts, which accounts for the absence of Eu anomalies in the amphibole (Fig. 10a). The lower Cr and Ni concentrations in amphibole of plagioclase hornblendite than those of hornblendite further suggest that the intergranular plagioclase originated from more evolved melts.

We simulated the crystallization sequence of the parental magma estimated for the Liuying complex (Table S9) using the rhyolite-MELTS program (Ghiorso and Sack, 1995) at 600 MPa and $\Delta NNO + 1$ oxidation state. Under these conditions, amphibole crystallization initiates at ∼ 900 °C. Modeled mineral compositions align with observed phases: amphibole exhibits $Mg^{\#}$ values of 71–82, while plagioclase an content decreases from 89 to 73. Within the complex, systematic compositional variations in amphibole and plagioclase suggest progressive crystallization within their stability field. Early removal of anhydrous phases elevated melt H_2O content, amplifying amphibole crystallization while inhibiting plagioclase nucleation. This process likely produce the Liuying hornblendite cumulates at higher temperatures and pressures (572–996 °C, 517–600 MPa), characterized by higher $Mg^{\#}$ of amphibole (76–81). Subsequently, the evolved melt promoted interstitial plagioclase crystallization within the amphibole framework, ultimately forming plagioclase hornblendite with lower $Mg^{\#}$ of amphibole ($Mg^{\#} =$ 78–73, 972–982 °C, 493–583 MPa).

6.3.2. Metasomatized mantle source above a paleo-subduction zone

The hornblendite studied here exhibits geochemical characteristics typical of arc-related rocks, including enrichment in LILEs and depletion in HFSEs (Fig. 8). Trace element compositions of the parental magma were calculated from composition of amphibole and plagioclase (Langmuir et al., 1992):

$$C^{i}_{liquid} = \frac{C^{i}_{cumulate}}{D^{i}_{cumulate}}$$

where C^{i}_{liquid} is the concentration of trace element i in the equilibrium melt, $C^{i}_{cumulate}$ denotes the concentration in the cumulate, and $D^{i}_{cumulate}$ represents the whole-rock distribution coefficient for the cumulate mineral assemblages.

Partition coefficients for amphibole and plagioclase were sourced from the GERM Database. As shown in Fig. 15a, the calculated parental magma REE abundances exhibit highly fractionated patterns with strong LREE enrichment and HREE depletion. The spidergram (Fig. 15b) further reveals enrichment in LILEs (e.g., Rb, Ba, Th, Sr) and LREE, coupled with depletion in HFSEs (e.g., Nb, Ta, Zr, Hf), suggesting arc-type signatures. These features align with the cumulate line of descent of hydrous arc magmas (Müntener and Ulmer, 2018) (Fig. 7). The zircons analyzed in this study fall above the mantle-zircon array and are chemically similar to those of continental arc rocks (Fig. 14), suggesting

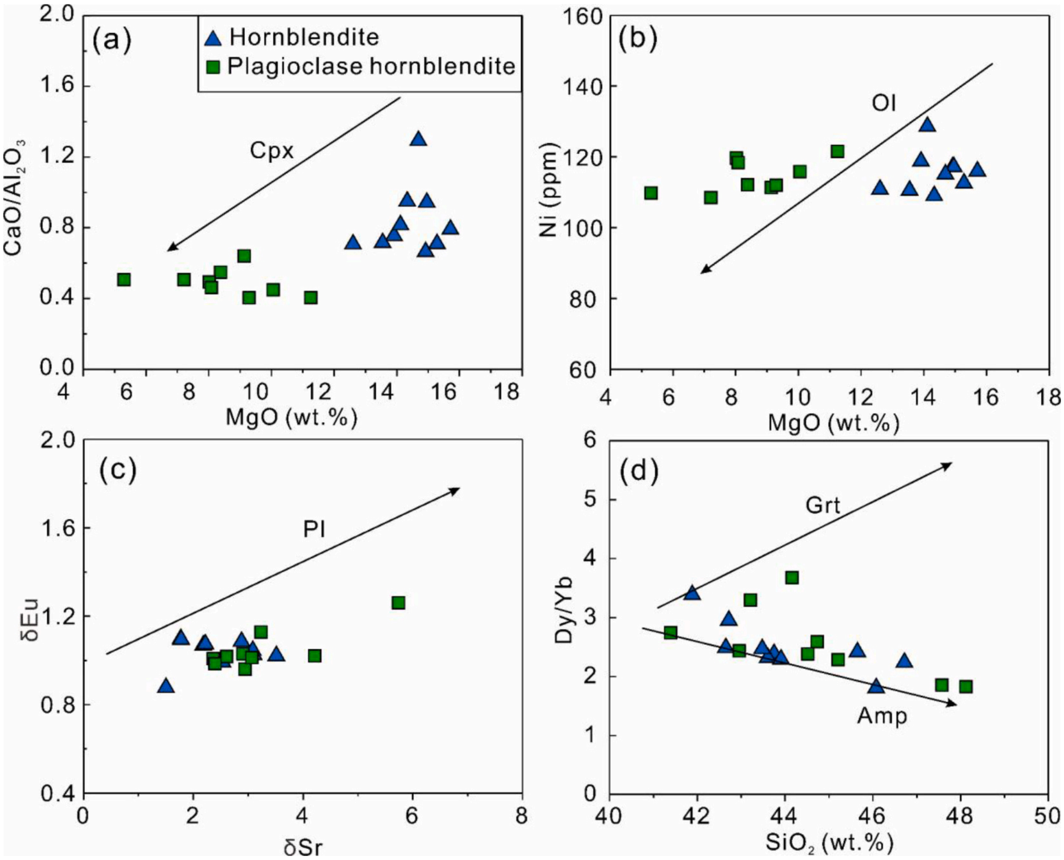

Fig. 13. (a) Plots of MgO contents versus CaO/Al$_2$O$_3$; (b) MgO contents versus Ni contents; (c) Sr/Sr* versus Eu/Eu*ratios; (d) SiO$_2$ contents versus Dy/Yb ratios for the Liuying ultramafic complex. Mineral abbreviations: Ol-olivine; Cpx-clinopyroxene; Pl-plagioclase; Grt-garnet; Amp-amphibole.

that the zircons crystallized from LILEs-enriched, hydrous mantle-derived magmas (Grimes et al. 2015; Zhao et al., 2019). This provides evidence that the northern NCC was a continental arc situated above a paleo-subduction zone at ~ 2.20 Ga (See Fig. 16).

In arc settings, mantle wedges can be modified by fluids and/or melts released from subducted sediments and basaltic crust (Eiler et al. 2000, Eiler et al., 2005; Hanyu et al. 2006; Falloon et al. 2008; Hiess et al. 2009). Dehydration of the subducting slab and sedimentary/volcanic material in the subduction channel releases fluids that hydrate the mantle wedge and flux it with LILEs, leading to partial melting of mantle wedge. Continuous mantle wedge corner flow brings new mantle under hyper-solidus flow to be metasomatized by slab-derived melts and/or fluids (Zheng, 2019; Kusky and Wang, 2022). These processes gradually form a lower crust/upper mantle hydrous cumulate complex, such as hornblendite cumulates, derived from slab flux melting.

The Sr-Nd-Hf isotopic compositions of the hornblendite closely resemble, yet are more extreme than, the oceanic Enriched Mantle-I (EMI) endmember composition (Fig. 11a). EMI is characterized by very low ^{143}Nd/^{144}Nd and ^{206}Pb/^{204}Pb, along with intermediate ^{87}Sr/^{86}Sr ratios (Zindler and Hart, 1986), which have been interpreted as indicative of mantle metasomatism by anciently subducted materials. Ancient subduction events delivered continent-derived siliciclastic sediments to the lithospheric mantle, generating the EMI Sr–Nd–Pb isotopic signatures. The Liuying ultramafic rocks has (^{87}Sr/^{86}Sr)$_i$ ratios of 0.704185–0.705932, (^{87}Sr/^{86}Sr)$_{amp}$ ratios of 0.705110–0.705846, and low ε_{Nd}(t) values (−14.6 to −5.68).The ε_{Nd}(t) values decouple from magmatic zircon ε_{Hf}(t) values of −5.96 to +3.17, and fall above the mantle-crustal array (Fig. 11d), suggesting that the mantle sources were fluxed by sediment-derived melts and fluids (Wang et al. 2014; Zhao et al., 2019). Oceanic sediment-derived melts can carry significant quantities of Nd and Hf, resulting in high Nd/Hf ratios and the decoupling of the Hf-Nd isotope systems, due to zircon sorting in terrigenous sediments during continental weathering (Chauvel et al. 2008), or the presence of residual zircon/rutile in subducted sediments (Tollstrup and Gill 2005). Calculations suggest that the ε_{Hf} and ε_{Nd} values of the hornblendite can be readily explained by mixing the mantle wedge with 5–10 % sediment-derived melts and fluids. Notably, 1.9–2.1 Ga metamorphic zircons exhibit higher ε_{Hf}(t) values (−1.40 to +9.05) than their 2.2–2.3 Ga counterparts. This Hf isotope dichotomy reflects two primary mechanisms: (i) Juvenile mantle input during post-collisional extension (1.95–1.80 Ga), evidenced by regional A-type granites with depleted mantle signatures (ε_{Hf}(t) = +2 to +8; Yang et al., 2012); (ii) Fluid-mediated recrystallization, where metasomatic fluids introduced mantle-derived Hf during retrogression. Resulting isotopic homogenization indicates open-system behavior via dissolution-reprecipitation processes.

6.4. *Tectonic implication for the northern NCC*

The ~ 2.2 Ga Liuying hornblendite arc cumulates provide confirmation that modern-style plate subduction and continental arc magmatism operated along the northern NCC as early as ~ 2.2 Ga, with the mantle wedge metasomatized by subducted slab-derived crustal materials. Previous studies have documented subduction-related Paleoproterozoic magmatism, including rocks with characteristics of typical “normal” arc volcanics in the Lüliang Massif (ca. 2.2 Ga, Liu et al 2014), ca. 1.9 Ga supra-subduction zone-type ophiolites in Bayan Obo (Wu et al., 2022), and ca. 2.15 Ga arc-type granites (Liu et al., 2009). Paleoproterozoic subduction zone beneath the northern NCC is further supported by high-pressure/temperature-type eclogite metamorphism at >1.88 Ga, along with ~1.90 Ga ophiolitic mélanges (Wei et al., 2023). Xu et al. (2017, Xu et al., 2018, Xu et al., 2019) and Wan et al. (2020)

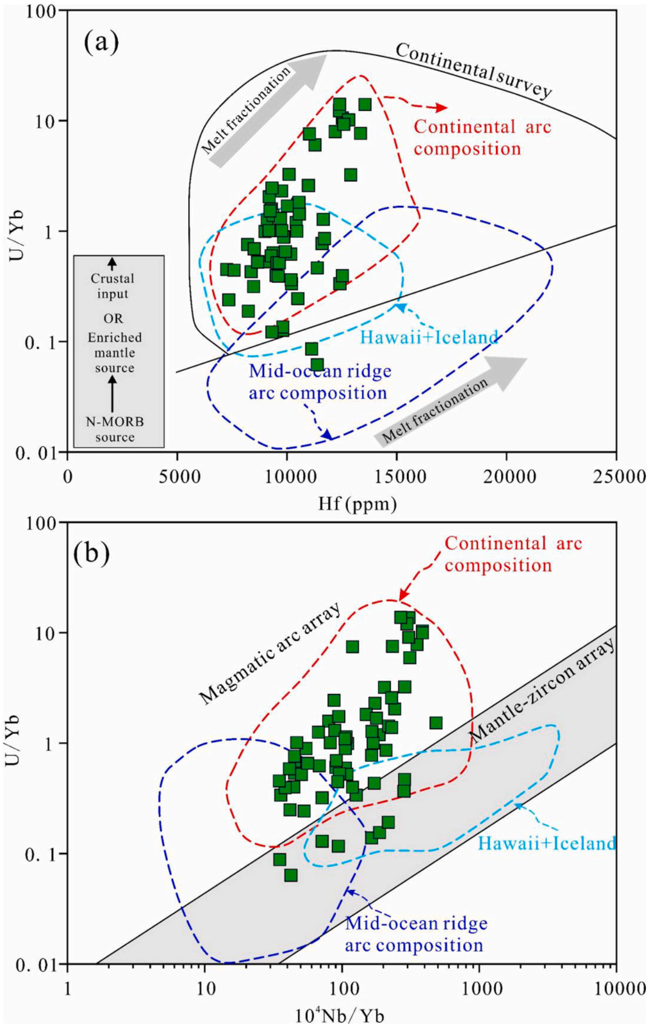

Fig. 14. Plots of Hf and 10^4Nb/Yb against U/Yb for the magmatic zircons with concordant ages from the Liuying hornblendite. The reference fields are from Grimes et al. (2015).

have also suggested that the northern NCC experienced modern-style subduction during the Paleoproterozoic, with the lithospheric mantle metasomatized by subducted sediment melts and fluids.

Three interpretations have been proposed regarding the Paleoproterozoic subduction system of the northern NCC. The first suggests that a subduction-collision event developed between an ancient continental block, known as the Fuping Block, and the Eastern Block, during the period from 2.12 to 1.98 Ga along the northern TNCO (Faure et al., 2007; Trap et al., 2012). However, evidence for the destruction of Fuping Block during amalgamation is spare (Zhao et al., 2012). Furthermore, the volume of the Fuping Block components (>2600 Ma), as indicated by detrital zircons, constitutes only ~ 10 % of the TNCO (Fig. 1) (Zhang et al., 2023). An alternative interpretation suggests that the Eastern Block acted as a long-lived (~700 Ma) continental margin arc from the late Neoarchean to Paleoproterozoic (Zhao et al., 2001, 2002, 2005, 2012; Wilde et al., 2002), followed by the collision between the Eastern Block and Western Block at ca. 1.95–1.85 Ga, forming the TNCO. This model is generally supported by “clockwise” pressure–temperature-time (P-T-t) paths for metamorphic rocks within the TNCO, dated to 1.90–1.85 Ga. Wei et al. (2023) provides an overview of recent metamorphic studies in the northern NCC, proposing that metamorphism during 1.94–1.90 Ga was a low-P/T event, characterized by ultrahigh-temperature granulite. This metamorphism is thought to result from conductive and advective heating from mantle upwelling and hyperthermal mafic magma underplating in a post-orogenic setting with back-arc extension. However, Kusky et al. (2016) and Xiao et al. (2021) argued that the P-T-t paths (1.90–1.85 Ga) primarily represent isothermal decompression paths, and likely bear no relation to earlier 2.5 Ga metamorphic events. Additionally, the ca. 1.90–1.80 Ga metamorphic events are documented throughout the NCC and is strongly recorded in rocks along the north margin of the craton rather than being confined to the TNCO (e.g., Peng et al., 2014; Kusky et al., 2016; Xiao et al., 2021; Zhang et al., 2023).

Notably, arc-type magmatism (plutonism and volcanism) from 2.3 to 1.85 Ga affected large portions of the northern, central, and western NCC, as well as the northern part of the eastern NCC (Zhao et al., 2005, 2012; Zhao and Zhai, 2013). Kusky et al. (2016) compared the scales of deformation, volcanism, and plutonism in the Cordilleran Ribbon Continent before its accretion to North America, and the Andes, to the NCC between 2.3 and 1.95 Ga, proposing that the northern NCC functioned as an Andean-type continental margin. A significant extension occurred in the upper plate during Andean-type subduction along the northern NCC, resulting in the formation of 2.2–2.0 Ga ultramafic–mafic intrusions, A-type granites and contemporaneous mafic dykes/sills (Zhao et al., 2011; Peng et al., 2012, 2014; Du et al., 2016; Wang et al., 2020; Liu et al., 2014). Zhang et al. (2023) argue that the concurrence of arc-type magmas and extension-related plutons, aligned in an east–west belt across the IMNHO or south of the NCC, is most consistent with the extensional *retro*-arc basin model proposed by Kusky et al. (2016). The

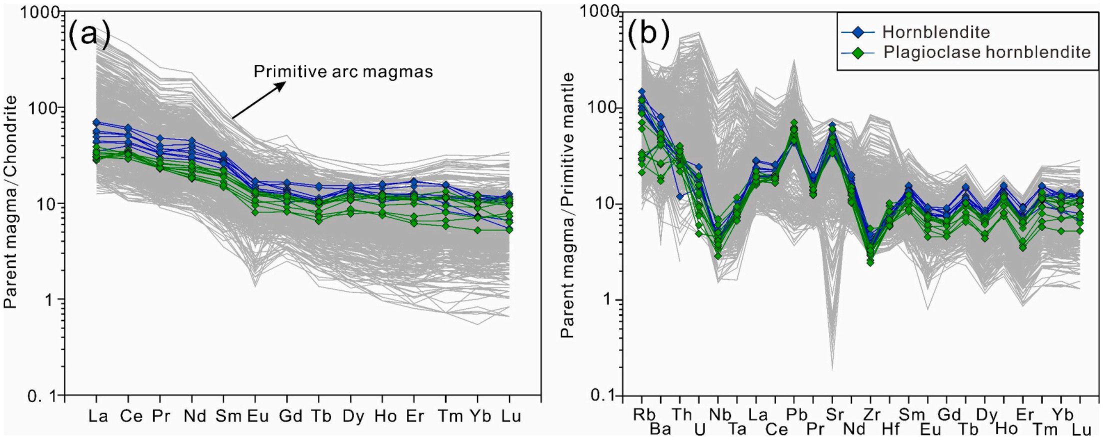

Fig. 15. Parental magma compositions (REEs and other trace elements) calculated from trace element abundances in amphibole. The trace elements of primitive arc magmas were from Chen et al. (2020), Greene et al. (2006), Mullen et al. (2017), Rosenbaum et al. (2021), Zhu et al. (2024). The normalization values for chondrite and primitive mantle are taken from McDonough et al. (1995).

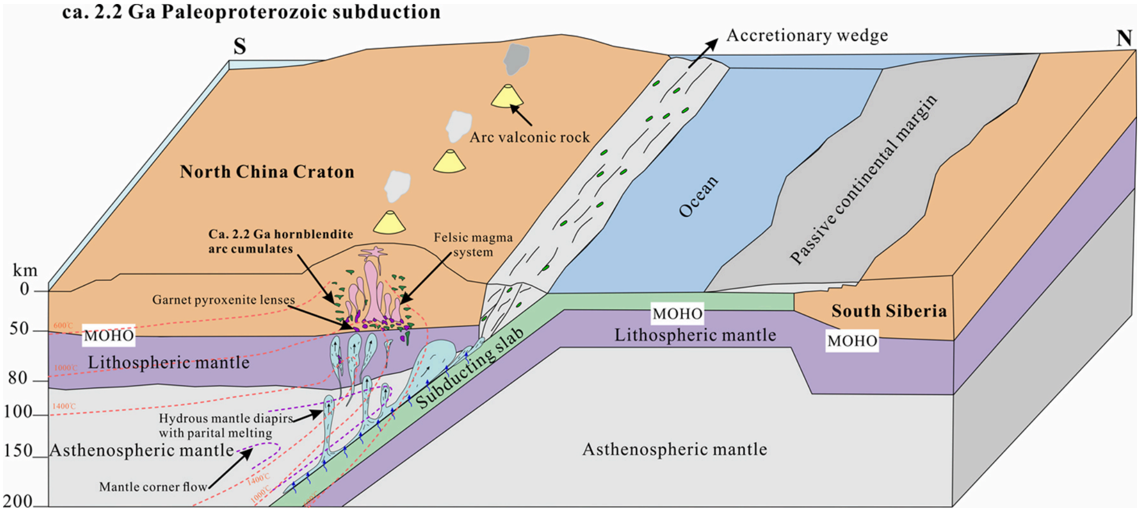

Fig. 16. Model of the structural and petrological processes in the thickened continental margin arc and subduction system of the northern North China Craton at ca. 2.2 Ga.

deformation within the IMNHO is characterized by roughly east–west-striking shear zones and folds, which are related to the south- and southeast- thrusting of the northern IMNHO over the NCC, followed by the collision between the NCC and the Columbian supercontinent along the IMNHO (Kusky et al., 2016). An arc sequence, constructed on older basement rocks (Kusky and Li, 2003), is represented by ca. 2.39 Ga granitoids in the Guyang and Chifeng metamorphic complexes of the Yinshan Block (Kusky et al., 2016). An accretionary wedge developed outboard of this arc, starting at ca. 2.3 Ga, as the northern NCC evolved into an Andean arc margin (Kusky and Li, 2003; Kusky et al., 2016).

Magmatism along convergent continental arc system generally occurs in pulses (magmatic flare-ups or magmatic lulls), which are reflected in the isotopic characteristics of arc magmas over time, such as initial ε_{Nd} and ε_{Hf} values (Paterson and Ducea, 2015). Negative $\varepsilon_{Hf}(t)$ excursions representing shortening and increased crustal melting over the duration of each flare-up. The intervening magmatic lulls are accompanied by rapid positive $\varepsilon_{Hf}(t)$ excursions signifying influxes of juvenile magma into the arc, probably during extension and foundering of underlying melt residua (Cope, 2017). The U-Pb chronology and Lu-Hf isotope data of Archean-Paleoproterozoic detrital zircons with igneous origin (Th/U ratio > 0.1) from the northern NCC show two negative $\varepsilon_{Hf}(t)$ excursions (trend A: 2.6–2.3 Ga, and trend B, 2.1–1.7 Ga) and one positive $\varepsilon_{Hf}(t)$ excursions (2.3–2.1 Ga) (Fig. 12). This cyclic magmatism is closely related to the Precambrian plate tectonic history of the northern NCC. The passive margin of the northern NCC was first disrupted by subduction and collision of intra-oceanic islands at ca. 2.6 Ga (Kusky et al., 2014; Wu et al., 2022). During 2.6–2.3 Ga, persistent subduction and collision of intro-oceanic islands along the northern NCC formed a ribbon continental margin arc (Kusky et al., 2007; Kusky and Santosh, 2009; Wu et al., 2022), as recorded by trend A, which suggests orogenic affinity and continuous crustal shortening. Between 2.3–2.1 Ga, the northern NCC entered a paleo-subduction continental arc setting, with widespread arc magmatism, including the ca. 2.2 Ga Liuying hornblendite arc cumulates. This period was marked by an intervening magmatic lull with rapid positive $\varepsilon_{Hf}(t)$, resulting from significant influxes of juvenile mantle-derived melts into arc and crustal thickening (Fig. 12). Similarly, the estimated crustal profile of the Cordillera Zealandia arc system after magma flare-ups is about 80 km, higher than the pre-flare-ups value of 48 km (Milan et al., 2017). The end of trend A likely corresponds to the collision between the northern NCC and the Siberian segment of the Columbia Supercontinent (Kusky and Santosh, 2009; Kusky et al., 2016), suggesting that the northern NCC participated in the formation and fragmentation of the Columbia supercontinent. During 2.1–1.7 Ga, the northern NCC shows collision-post orogenic affinity, with widespread tectonic-thermal events, forming the ca. 1.95 Ga metamorphic zircons of the Liuying cumulates.

7. Conclusion

The Liuying ultramafic complex, dominated by amphibole with subordinate plagioclase, exhibits magmatic cumulate texture and was emplaced at ca. 2.2 Ga. It formed through fractional crystallization of hydrous arc magmas at middle-lower crust (18–23 km depth) at 966–996 °C. The rocks show arc-affinity geochemical signatures characterized by enrichment in large-ion lithophile elements and depletion in high-field strength elements. Enriched Sr-Nd isotopic compositions decoupled from depleted zircon Hf isotope, confirming a subduction-modified lithospheric mantle source. The mantle source was mixed with 5–10 % sediment-derived melts and fluids. At ca. 2.2 Ga, the northern part of the North China Craton constituted a continental arc above a paleo-subduction zone. During Columbia supercontinent assembly, southward subduction of an oceanic slab beneath the NCC margin triggered extensive melting of a metasomatized mantle wedge, generating Paleoproterozoic hornblendite-dominated arc cumulates.

CRediT authorship contribution statement

Wen-Mei Liu: Writing – original draft. **Jian-Ping Zheng:** Supervision, Resources. **Bernard Charlier:** Writing – review & editing. **Qiang Ma:** Writing – review & editing. **Timothy Kusky:** Writing – review & editing. **Hong-Kun Dai:** Writing – review & editing.

Declaration of competing interest

The authors declare that they have no known competing financial interests or personal relationships that could have appeared to influence the work reported in this paper.

Acknowledgements

We sincerely thank Dr. J. Zhang (Editor), Dr. C.R. Diwu (Assistant Editor), Dr. Z.W. Wang (Reviewer), and an anonymous reviewer for their insightful comments and suggestions, which greatly improved the clarity of the ideas presented in this study. We also thank Dr. W.B. Ning for his thoughtful discussion on some critical issues, also thank Dr. D. Zhang, Mr. Y.C. Li and L.F. Xue for the technical supports during the LA-ICP-MS U-Pb, in-situ Lu-Hf, and whole-rock major element analyses.

This work was supported by the National Key Research and Development Program of China (2023YFF0804404) and the Natural Science Foundation of China (No. 42320104001).

Appendix A. Supplementary data

Supplementary data to this article can be found online at https://doi.org/10.1016/j.precamres.2025.107946.

Data availability

Data will be made available on request.

References

Bizzarro, M., Simonetti, A., Stevenson, R.K., Kurszlaukis, S., 2003. In situ ^{87}Sr/^{86}Sr investigation of igneous apatites and carbonates using laser ablation MC-ICP-MS. Geochim. Cosmochim. Acta 67 (2), 289–302. https://doi.org/10.1016/S0016-7037(02)01048-7.

Cawood, P.A., Hawkesworth, C.J., Pisarevsky, S.A., Dhuime, B., Capitanio, F.A., Nebel, O., 2018. Geological archive of the onset of plate tectonics. Philosophical Transactions of the Royal Society, Series A, Mathematical: Physical and Engineering Sciences 376, 2132. https://doi.org/10.1098/rsta.2017.0405.

Chauvel, C., Lewin, E., Carpentier, M., Arndt, N.T., Marini, J.C., 2008. Role of recycled oceanic basalt and sediment in generating the Hf-Nd mantle array. Nat. Geosci. 1, 64–67. https://doi.org/10.1038/ngeo.2007.51.

Chen, K., Tang, M., Lee, C.-T.-A., Wang, Z., Zou, Z., Hu, Z., Liu, Y., 2020. Sulfide-bearing cumulates in deep continental arcs: the missing copper reservoir. Earth Planet. Sci. Lett. 531, 115971. https://doi.org/10.1016/j.epsl.2019.115971.

Cope, T., 2017. Phanerozoic magmatic tempos of North China. Earth Planet. Sci. Lett. 458, 1–10. https://doi.org/10.1016/j.epsl.2017.03.022.

Crisp, L.J., Berry, A.J., Burnham, A.D., Miller, L.A., Newville, M., 2023. The Ti-in-zircon thermometer revised: the effect of pressure on the Ti site in zircon. Geochim. Cosmochim. Acta 360, 241–258. https://doi.org/10.1016/j.gca.2023.04.031.

Daczko, N.R., Piazolo, S., Meek, U., Stuart, C.A., Elliott, V., 2016. Hornblendite delineates zones of mass transfer through the lower crust. Sci. Rep. 6, 1–6. https://doi.org/10.1038/srep31369.

Dai, H.K., Zheng, J.P., Griffin, W.L., O'Reilly, S.Y., Xiong, Q., Ping, X.Q., Chen, F.K., Lu, J.G., 2021. Pyroxenite Xenoliths Record complex Melt Impregnation in the Deep Lithosphere of the Northwestern North China Craton. J. Petrol. 62. https://doi.org/10.1093/petrology/egaa079.

Du, L., Yang, C., Wyman, D.A., Nutman, A.P., Lu, Z., Song, H., Xie, H., Wan, Y., Zhao, L., Geng, Y., Ren, L., 2016. 2090–2070Ma A-type granitoids in Zanhuang complex: further evidence on a Paleoproterozoic rift-related tectonic regime in the Trans-North China Orogen. Lithos 254–255, 18–35. https://doi.org/10.1016/j.lithos.2016.03.007.

Eiler, J.M., Crawford, A., Elliott, T., Farley, K.A., Valley, J.W., Stolper, E.M., 2000. Oxygen isotope geochemistry of oceanic-arc lavas. J. Petrol. 41, 229–256. https://doi.org/10.1093/petrology/41.2.229.

Eiler, J.M., Carr, M.J., Reagan, M., Stolper, E., 2005. Oxygen isotope constraints on the sources of central American arc lavas. Geochem Geophy Geosy 6, Q07007. https://doi.org/10.1029/2004GC000804.

Falloon, T., Danyushevsky, L.V., Crawford, A., Meffre, S., Woodhead, J.D., Bloomer, S.H., 2008. Boninites and adakites from the northern termination of the Tonga Trench: implications for adakite petro- genesis. J. Petrol. 49, 697–715. https://doi.org/10.1093/petrology/egm080.

Faure, M., Trap, P., Lin, W., Monie, P., Bruguier, O., 2007. Polyorogenic evolution of the Paleoproterozoic Trans-North China Belt, new insights from the Lüliangshan–Hengshan–Wutaishan and Fuping massifs. Episodes 30, 1–12. https://doi.org/10.18814/epiiugs/2007/v30i2/004.

Gale, A., Dalton, C.A., Langmuir, C.H., Su, Y., Schilling, J., 2013. The mean composition of ocean ridge basalts. Geochem Geophy Geosy 14, 489–518. https://doi.org/10.1029/2012GC004334.

Ghiorso, M.S., Sack, R.O., 1995. Chemical mass transfer in magmatic processes IV. a revised and internally consistent thermodynamic model for the interpolation and extrapolation of liquid-solid equilibria in magmatic systems at elevated temperatures and pressures. Contr. Mineral. and Petrol. 119, 197–212. https://doi.org/10.1007/BF00307281.

Greene, A.R., DeBari, S.M., Kelemen, P.B., Blusztain, J., Clift, P.D., 2006. A detailed geochemical study of island arc crust: the Talkeetna arc section, south-central Alaska. J. Petrol. 47 (6), 1051–1093. https://doi.org/10.1093/petrology/egl002.

Griffin, W.L., Wang, X., Jackson, S.E., Pearson, N.J., O'Reilly, S.Y., Xu, X.S., Zhou, X.M., 2002. Zircon chemistry and magma mixing, SE China: In-situ analysis of Hf isotopes, Tonglu and Pingtan igneous complexes. Lithos 61, 237–269. https://doi.org/10.1016/S0024-4937(02)00082-8.

Grimes, C.B., John, B.E., Cheadle, M.J., Frank, K., Mazdab, J.L., Wooden, S.S., Joshua, J. S., 2009. On the occurrence, trace element geochemistry, and crystallization history of zircon from in situ ocean lithosphere. Contrib. Miner. Petrol. 158, 757–783. https://doi.org/10.1007/s00410-009-0409-2.

Grimes, C.B., Wooden, J.L., Cheadle, M.J., John, B.E., 2015. "Fingerprinting" tectono-magmatic provenance using trace elements in igneous zircon. Contrib. Miner. Petrol. 170, 46. https://doi.org/10.1007/s00410-015-1199-3.

Guo, L., Jagoutz, O., Shinevar, W.J., Zhang, H.-F., 2020. Formation and composition of the late cretaceous Gangdese arc lower crust in southern Tibet. Contrib. Miner. Petrol. 175, 58. https://doi.org/10.1007/s00410-020-01696-y.

Hacker, B.R., Mehl, L., Kelemen, P.B., Rioux, M., Behn, M.D., Luffi, P., 2008. Reconstruction of the Talkeetna intraoceanic arc of Alaska through thermobarometry. J. Geophys. Res. 113, B03204. https://doi.org/10.1029/2007JB005208.

Hanyu, T., Tatsumi, Y., Nakai, S., Chang, Q., Miyazaki, T., Sato, K., Tani, K., Shibata, T., Yoshida, T., 2006. Contribution of slab melting and slab dehydration to magmatism in the NE Japan arc for the last 25 Myr: constraints from geochemistry. Geochem. Geophys. Geosyst. 7, Q08002. https://doi.org/10.1029/2005GC001220.

Hiess, J., Bennett, V.C., Nutman, A.P., Williams, I.S., 2009. In situ U–Pb, O and Hf isotopic compositions of zircon and olivine from Eoar-chaean rocks, West Greenland: new insights to making old crust. Geochim. Cosmochim. Acta 73, 4489–4516. https://doi.org/10.1016/j.gca.2009.04.019.

Hoskin, P.W.O., Schaltegger, U., 2003. The Composition of Zircon and Igneous and Metamorphic Petrogenesis. Rev. Mineral. Geochem. 53 (1), 27–62. https://doi.org/10.2113/0530027.

Itano, K., Takehara, M., Horie, K., Iizuka, T., Nishio, I., Morishita, T., 2024. A long-lived mafic magma reservoir: Zircon evidence from a hornblende peridotite in the Hida Belt, Japan. Geology 52, 3–6. https://doi.org/10.1130/G51560.1.

Jagoutz, O., 2014. Arc crustal differentiation mechanisms. Earth Planet. Sci. Lett. 396, 267–277. https://doi.org/10.1016/j.epsl.2014.03.060.

Jagoutz, O., Muntener, O., Burg, J.P., Ulmer, P., Jagoutz, E., 2006. Lower continental crust formation through focused flow in km-scale melt conduits: the zoned ultramafic bodies of the Chilas complex in the Kohistan island arc (NW Pakistan). Earth Planet. Sci. Lett. 242 (3–4), 320–342. https://doi.org/10.1016/j.epsl.2005.12.005.

Jagoutz, O., Mütener, O., Schmidt, M.W., Burg, J.P., 2011. The roles of flux- and decompression melting and their respective fractionation lines for continental crust formation: evidence from the Kohistan arc. Earth Planet. Sci. Lett. 303 (1–2), 25–36. https://doi.org/10.1016/j.epsl.2010.12.017.

Kelemen, P.B., Hanghøj, K., Greene, A.R., 2003. One View of the Geochemistry of Subduction-Related Magmatic Arcs, with an Emphasis on Primitive Andesite and lower Crust. Treat. Geochem. 3, 749–806. https://doi.org/10.1016/B0-08-043751-6/03035-8.

Korenaga, J., 2013. Initiation and evolution of plate tectonics on Earth: Theories and observations. Annu Rev Earth Pl Sc 41, 117–151. https://doi.org/10.1146/annurev-earth-050212-124208.

Kusky, T.M., 2011. Geophysical and geological tests of tectonic models of the North China Craton. Gondw. Res. 20, 26–35. https://doi.org/10.1016/j.gr.2011.01.004.

Kusky, T.M., Li, J.H., 2003. Paleoproterozoic tectonic evolution of the North China craton. J. Asian Earth Sci. 22 (4), 383–397. https://doi.org/10.1016/S1367-9120(03)00071-3.

Kusky, T.M., Mooney, W.D., 2015. Is the Ordos Basin floored by a trapped oceanic plateau? Earth Planet. Sci. Lett. 429, 197–204. https://doi.org/10.1016/j.epsl.2015.07.069.

Kusky, T.M., Santosh, M., 2009. The Columbia connection in North China. 323, 49–71. https://doi.org/10.1144/SP323.3.

Kusky, T.M., Wang, L., 2022. Growth of continental crust in intra-oceanic and continental-margin arc systems: Analogs for Archean systems. Sci. China Earth Sci. 65, 1615–1645. https://doi.org/10.1007/s11430-021-9964-1.

Kusky, T.M., Li, J.H., Santosh, M., 2007. The Paleoproterozoic North Hebei orogen: North China craton's collisional suture with the Columbia supercontinent. Gondw. Res. 12 (1–2), 4–28. https://doi.org/10.1016/j.gr.2006.11.012.

Kusky, T.M., Windley, B.F., Wang, L., Wang, Z.S., Li, X.Y., Zhu, P.M., 2014. Flat slab subduction, trench suction, and craton destruction: Comparison of the North China, Wyoming, and Brazilian cratons. Tectonophysics 630, 208–221. https://doi.org/10.1016/j.tecto.2014.05.028.

Kusky, T.M., Polat, A., Polat, A., Windley, B.F., Windley, B.F., Burke, K.C., Dewey, J.F., Kidd, W.S., Maruyama, S., Maruyama, S., Wang, J., Deng, H., Wang, Z., Wang, C., Fu, D., Li, X., Peng, H., 2016. Insights into the tectonic evolution of the North China Craton through comparative tectonic analysis: a record of outward growth of Precambrian continents. Earth Sci. Rev. 162, 387–432. https://doi.org/10.1016/j.earscirev.2016.09.002.

Langmuir, C.H., Klein, E.M., Plank, T., 1992. Petrological systematics of mid-ocean ridge basalts: constraints on melt generation beneath ocean ridges. Geophysical monograph series 71, 183–280. https://doi.org/10.1029/GM071p0183.

Leake, B.E., Woolley, A.R., Arps, C.E., Birch, W.D., Gilbert, M.C., Grice, J.D., Hawthorne, F.C., Kato, A., Kisch, H.J., Krivovichev, V.G., Linthout, K., Laird, J.O., Mandarino, J., Maresch, W.V., Nickel, E.H., Rock, N.M., Schumacher, J.C., Smith, D. C., Stephenson, N.C., Ungaretti, L., Whittaker, E.J., Youzhi, G., 1997. Nomenclature of Amphiboles; Report of the Subcommittee on Amphiboles of the International Mineralogical Association Commission on New Minerals and Mineral Names. Mineral. Mag. 61, 295–310. https://doi.org/10.1180/minmag.1997.061.405.13.

Li, X.H., Long, W.G., Li, Q.L., Liu, Y., Zheng, Y.F., Yang, Y.H., Chamberlain, K.R., Wan, D. F., Guo, C.H., Wang, X.C., Tao, H., 2010. Penglai zircon megacrysts: a potential new working reference material for microbeam determination of Hf-O isotopes and U-Pb age. Geostand. Geoanal. Res. 34, 117–134. https://doi.org/10.1111/j.1751-908X.2010.00036.x.

Liu, S., Li, Q., Liu, C., Lv, Y., Zhang, F., 2009. Guandishan granitoids of the Paleoproterozoic Lüliang metamorphic complex in the Trans-North China Orogen: SHRIMP zircon ages, petrogenesis and tectonic implications. Acta Geol. Sin.-Engl. Ed. 83 (3), 580–602.

Liu, C., Zhao, G., Liu, F., Shi, J., 2014. 2.2 Ga magnesian andesites, Nb-enriched basalt-andesites, and adakitic rocks in the Lüliang complex: evidence for early

Paleoproterozoic subduction in the North China Craton. Lithos 208–209, 104–117. https://doi.org/10.1016/j.lithos.2014.08.025.

Liu, S., Fu, J., Lu, Y.J., Chen, X., Wang, M., Hu, F., Gao, L., Sun, G., Hu, Y., 2019. Precambrian Hongqiyingzi complex at the northern margin of the North China Craton: its zircon U-Pb-Hf systematics, geochemistry and constraints on crustal evolution. Precambr. Res. 326, 58–83. https://doi.org/10.1016/j.precamres.2018.05.019.

Liu, W.M., Zheng, J.P., Charlier, B., Ma, Q., Dai, H.K., 2024. Genesis of the Devonian Habaqin ultramafic arc complex and associated low-grade Fe–Ti oxide mineralization in the northern North China Craton. Lithos 478–479, 107625. https://doi.org/10.1016/j.lithos.2024.107625.

Ludwig, K.R., 2003. Isoplot 3.00: a Geochronological Toolkit for Microsoft Excel. Berkeley Geochronology Center Special Publication 4.

Ma, X., Chen, B., Chen, J.F., Niu, X.L., 2013. Zircon SHRIMP U-Pb age, geochemical, Sr-Nd isotopic, and in-situ Hf isotopic data of the late Carboniferous-Early Permian plutons in the northern margin of the North China Craton. Sci. China Earth Sci. 56, 126–144. https://doi.org/10.1007/s11430-012-4456-6.

McDonough, W.F., Sun, S.S., 1995. The composition of the Earth. Chem. Geol. 120, 223–253. https://doi.org/10.1016/0009-2541(94)00140-4.

Milan, L.A., Daczko, N.R., Clarke, G.L., 2017. Cordillera Zealandia: a Mesozoic arc flare-up on the Paleo-Pacific Gondwana Margin. Sci. Rep. 7, 261. https://doi.org/10.1038/s41598-017-00347-w.

Mullen, E.K., Weis, D., Marsh, N.B., Martindale, M., 2017. Primitive arc magma diversity: New geochemical insights in the Cascade Arc. Chem. Geol. 448, 43–70. https://doi.org/10.1016/j.chemgeo.2016.11.006.

Müntener, O., Ulmer, P., 2018. Arc crust formation and differentiation constrained by experimental petrology. Am. J. Sci. 318, 64–89. https://doi.org/10.2475/01.2018.04.

Müntener, O., Kelemen, P., Grove, T., 2001. The role of H_2O during crystallization of primitive arc magmas under uppermost mantle conditions and genesis of igneous pyroxenites: an experimental study. Contrib. Miner. Petrol. 141, 643–658. https://doi.org/10.1007/s004100100266.

Ning, W.B., Kusky, T.M., Wang, L., Huang, B., 2022. Archean eclogite-facies oceanic crust indicates modern-style plate tectonics. PNAS 119 (15), e2117529119. https://doi.org/10.1073/pnas.211752911.

Paterson, S.R., Ducea, M.N., 2015. Arc magmatic tempos: Gathering the evidence. Elements 11, 91–98. https://doi.org/10.2113/gselements.11.2.91.

Peng, P., Guo, J., Zhai, M., Windley, B.F., Li, T., Liu, F., 2012. Genesis of the Hengling magmatic belt in the North China Craton: Implications for Paleoproterozoic tectonics. Lithos 148, 27–44. https://doi.org/10.1016/j.lithos.2012.05.021.

Peng, P., Wang, X.P., Windley, B.F., Guo, J.H., Zhai, M.G., Li, Y., 2014. Spatial distribution of ~1950–1800 Ma metamorphic events in the North China craton: Implications for tectonic subdivision of the craton. Lithos 202–203, 250–266. https://doi.org/10.1016/j.lithos.2014.05.033.

Plank, T., 2014. The Chemical Composition of Subducting Sediments. In: Treatise on Geochemistry. Elsevier, pp. 607–629. https://doi.org/10.1016/B978-0-08-095975-7.00319-3.

Ridolfi, F., Renzulli, A., Puerini, M., 2010. Stability and chemical equilibrium of amphibole in calc-alkaline magmas: an overview, new thermobarometric formulations and application to subduction-related volcanoes. Contrib. Miner. Petrol. 160 (1), 45–66. https://doi.org/10.1007/s00410-009-0465-7.

Rioux, M., Hacker, B., Mattinson, J., Kelemen, P., Blusztajn, J., Gehrels, G., 2007. The magmatic development of an intra-oceanic arc: High-precision U-Pb zircon and whole-rock isotopic analyses from the accreted Talkeetna arc, south-central Alaska. Geol. Soc. Am. Bull. 119 (9–10), 1168–1184. https://doi.org/10.1130/B25964.1.

Rioux, M., Mattinson, J., Hacker, B., Kelemen, P., Blusztajn, J., Hanghøj, K., Gehrels, G., 2010. Intermediate to felsic middle crust in the accreted Talkeetna arc, the Alaska Peninsula and Kodiak Island, Alaska: an analogue for low–velocity middle crust in modern arcs. Tectonics 29 (3), TC3001. https://doi.org/10.1029/2009TC002541.

Rosenbaum, G., Caulfield, J.T., Ubide, T., Ward, J.F., Sandiford, D., Sandiford, M., 2021. Spatially and geochemically anomalous arc magmatism: Insights from the andean arc. Geochem. Geophys. Geosyst. 22, e2021GC009688. https://doi.org/10.1029/2021GC009688.

Salters, V.J.M., Stracke, A., 2004. Composition of the depleted mantle. Geochem. Geophys. Geosyst. 5. https://doi.org/10.1029/2003GC000597.

Santosh, M., Tsunogae, T., Li, J., Liu, S., 2007a. Discovery of sapphirine-bearing Mg–Al granulites in the North China Craton: Implications for Paleoproterozoic ultrahigh temperature metamorphism. Gondw. Res. 11, 263–285. https://doi.org/10.1016/j.gr.2006.10.009.

Santosh, M., Wilde, S.A., Li, J.H., 2007b. Timing of Paleoproterozoic ultrahigh-temperature metamorphism in the North China Craton: evidence from SHRIMP U–Pb zircon geochronology. Precambr. Res. 159 (3–4), 178–196. https://doi.org/10.1016/j.precamres.2007.06.006.

Smith, D.J., 2014. Clinopyroxene precursors to amphibole sponge in arc crust. Nat. Commun. 5, 4329. https://doi.org/10.1038/ncomms5329.

Song, B., Nutman, A.P., Liu, D.Y., Wu, J.S., 1996. 3800 to 2500 crustal evolution in the Anshan area of Liaoning Province, northeastern North China. Precambr. Res. 78, 79–94. https://doi.org/10.1016/0301-9268(95)00070-4.

Sun, D., Li, Q., Liu, S., Chen, X., Wang, Z., Chen, Y., Cao, S., Wang, X., 2019. Neoarchean-Paleoproterozoic magmatic arc evolution in the Wutai-Hengshan-Fuping area, North China Craton: New perspectives from zircon U–Pb ages and Hf isotopic data. Precambr. Res. 331, 105368. https://doi.org/10.1016/j.precamres.2019.105368.

Sun, G.Z., Liu, S.W., Cawood, P., Tang, M., van Hunen, J., Gao, L., Hu, Y.L., Hu, F.Y., 2021. Thermal state and evolving geodynamic regimes of the Meso- to Neoarchean North China Craton. Nat. Commun 12, 3888. https://doi.org/10.1038/s41467-021-24139-z.

Teng, X.M., Yang, Q.Y., Santosh, M., 2015. Devonian magmatism associated with arc-continent collision in the northern North China Craton: evidence from the Longwangmiao ultramafic intrusion in the Damiao area. J. Asian Earth Sci. 113, 626–643. https://doi.org/10.1016/j.jseaes.2015.04.032.

Tollstrup, D.L., Gill, J.B., 2005. Hafnium systematics of the Mariana arc: evidence for sediment melt and residual phases. Geology 33, 737–740. https://doi.org/10.1130/G21639.1.

Trap, P., Faure, M., Lin, W., Le Breton, N., Monie, P., 2012. Paleoproterozoic tectonic evolution of the Trans-North China orogen: Toward a comprehensive model. Precambr. Res. 222–223, 191–211. https://doi.org/10.1016/j.precamres.2011.09.008.

Triantafyllou, A., Berger, J., Baele, J.M., Bruguier, O., Diot, H., Ennih, N., Monnier, C., Plissart, G., Vandycke, S., Watlet, A., 2018. Intra-oceanic arc growth driven by magmatic and tectonic processes recorded in the Neoproterozoic Bougmane arc complex (Anti-Atlas, Morocco). Precambr. Res. 304, 39–63. https://doi.org/10.1016/j.precamres.2017.10.022.

Wan, B., Windley, B.F., Xiao, W., Feng, J., Zhang, J., 2015. Paleoproterozoic high-pressure metamorphism in the northern North China craton and implications for the Nuna supercontinent. Nat. Commun. 6 (1), 8344. https://doi.org/10.1038/ncomms9344.

Wan, B., Yang, X., Tian, X., Yuan, H., Kirscher, U., Mitchell, R.N., 2020. Seismological evidence for the earliest global subduction network at 2 Ga ago. Sci. Adv. 6, 1–9. https://doi.org/10.1126/sciadv.abc5491.

Wang, J., Kusky, T., Polat, A., Wang, L., Deng, H., Wang, S., 2013. A late Archean tectonic mélange in the Central orogenic belt, North China craton. Tectonophysics 608, 929–946. https://doi.org/10.1016/j.tecto.2013.07.025.

Wang, H., Wu, Y.B., Li, C.R., Zhao, T.Y., Qin, Z.W., Zhu, L.Q., Gao, S., Zheng, J.P., Liu, X.M., Zhou, L., Zhang, Y., Yang, S.H., 2014. Recycling of sediment into the mantle source of K-rich mafic rocks: Sr–Nd–Hf–O isotopic evidence from the Fushui complex in the Qinling Orogen. Contrib. Miner. Petrol. 168, 1062. https://doi.org/10.1007/s00410-014-1062-y.

Wang, J.P., Kusky, T., Wang, L., Polat, A., Deng, H., Wang, C., Wang, S.J., 2017. Structural relationships along a Neoarchean arc-continent collision zone, North China craton. GSA Bull. 129 (1–2), 59–75. https://doi.org/10.1130/B31479.1.

Wang, J.P., Li, X.W., Ning, W.B., Kusky, T., Wang, L., Polat, A., Deng, H., 2019. Geology of a Neoarchean suture: evidence from the Zunhua ophiolitic mélange of the Eastern Hebei Province, North China Craton. GSA Bull. 131, 1943–1964. https://doi.org/10.1130/B35138.1.

Wang, J., Yang, C., Wyman, D.A., Song, H., Du, L., 2020. Petrogenesis and tectonic implications of the 2.1–2.0 Ga granitoids in Fuping complex, North China Craton: Constraints from petrology, geochemistry and zircon U-Pb-Hf isotopes. Precambr. Res. 386–387, 106007. https://doi.org/10.1016/j.lithos.2021.106007.

Watson, E.B., Harrison, T.M., 2005. Zircon Thermometer Reveals Minimum Melting Conditions on Earliest Earth. Science 308, 841–844. https://doi.org/10.1126/science.1110873.

Wei, C.J., Zhai, M.G., Wang, B., 2023. Four phases of Orosirian metamorphism in the north North China Craton (NNCC): Insights into the regional tectonic framework and evolution. Earth Sci. Rev. 241. https://doi.org/10.1016/j.earscirev.2023.104449.

Wiedenbeck, M., Hanchar, J.M., Peck, W.H., Sylvester, P., Valley, J., Whitehouse, M., Kronz, A., Morishita, Y., Nasdala, L., et al., 2004. Further characterisation of the 91500 zircon crystal. Geostand. Geoanal. Res. 28, 9–39. https://doi.org/10.1111/j.1751-908X.2004.tb01041.x.

Wilde, S.A., Zhao, G.C., Sun, M., 2002. Development of the North China Craton during the late Archean and its final amalgamation at 1.8 Ga: some speculation on its position within a global Paleoproterozoic supercontinent. Gondw. Res. 5, 85–94. https://doi.org/10.1016/S1342-937X(05)70892-3.

Wu, C., Zhou, Z.G., Zuza, A.V., Wang, G.S., Liu, C.F., Jiang, T., 2018. A 1.9 Ga mélange along the northern margin of the North China craton: Implications for the assembly of Columbia supercontinent. Tectonics 37, 3610–3646. https://doi.org/10.1029/2018TC005103.

Wu, C., Wang, G., Zhou, Z., Haproff, P.J., Zuza, A.V., Liu, W., 2022. Paleoproterozoic Plate Tectonics Recorded in the Northern Margin Orogen, North China Craton. Geochem. Geophys. Geosyst. 23, 11. https://doi.org/10.1029/2022GC010662.

Wu, C., Wang, G., Zhou, Z., Zhao, X., Haproff, P.J., 2023. Late Archean–Paleoproterozoic plate tectonics along the northern margin of the North China craton. GSA Bull. 135 (3–4), 967–989. https://doi.org/10.1130/B36533.1.

Xiao, W.J., Windley, B.F., Sun, S., Li, J.L., Huang, B.C., Han, C.M., Yuan, C., Sun, M., Chen, H.L., 2015. A tale of amalgamation of three Permo-Triassic college Systems in Central Asia: Oroclines, Sutures, and Terminal Accretion. Annu Rev Earth Pl Sc 43, 477–507. https://doi.org/10.1146/annurev-earth-060614-105254.

Xiao, D., Ning, W., Wang, J., Kusky, T., Wang, L., Deng, H., Zhong, Y., Jiang, K., 2021. Neoarchean to Paleoproterozoic tectonothermal evolution of the North China Craton: constraints from geological mapping and Th-U-Pb geochronology of zircon, titanite and monazite in Zanhuang Massif. Precambr. Res. 359, 106214. https://doi.org/10.1016/j.precamres.2021.106214.

Xu, C., Kynický, J., Tao, R., Liu, X., Zhang, L., Pohanka, M., Song, W., Fei, Y., 2017. Recovery of an oxidized majorite inclusion from Earth's deep asthenosphere. Sci. Adv. 3, 1–6. https://doi.org/10.1126/sciadv.1601589.

Xu, C., Kynický, J., Song, W., Tao, R., Lü, Z., Li, Y., Yang, Y., Pohanka, M., Galiova, M.V., Zhang, L., Fei, Y., 2018. Cold deep subduction recorded by remnants of a Paleoproterozoic carbonated slab. Nat. Commun. 9, 1–8. https://doi.org/10.1038/s41467-018-05140-5.

Xu, C., Chakhmouradian, A.R., Kynický, J., Li, Y., Song, W., Chen, W., 2019. A Paleoproterozoic mantle source modified by subducted sediments under the North

China craton. Geochim. Cosmochim. Acta 245, 222–239. https://doi.org/10.1016/j.gca.2018.10.032.

Yang, J.H., Sun, J.F., Zhang, J.H., Wilde, S.A., 2012. Petrogenesis of late Triassic intrusive rocks in the northern Liaodong Peninsula related to decratonization of the North China Craton: Zircon U–Pb age and Hf–O isotope evidence. Lithos 153, 108–128. https://doi.org/10.1016/j.lithos.2012.06.023.

Yin, A., Brandl, G., Kröner, A., 2020. Plate-tectonic processes at ca. 2.0 Ga: Evidence from >600 km of plate convergence. Geology 48 (2), 103–107. https://doi.org/10.1130/G47070.1.

Zhai, M.G., Zhao, L., Zhu, X., Zhou, Y., Peng, P., Guo, J., Li, X., 2021. Late Neoarchean magmatic-metamorphic event and crustal stabilization in the North China Craton. Am J Sci 321 (1–2), 206–234. https://doi.org/10.2475/01.2021.06.

Zhang, S.H., Liu, S.W., Zhao, Y., Yang, J.H., Song, B., Liu, X.M., 2007. The 1.75–1.68 Ga anorthosite-mangerite-alkali granitoid-rapakivi granite suite from the northern North China Craton: Magmatism related to a Paleoproterozoic orogen. Precambr. Res. 155 (3–4), 287–312. https://doi.org/10.1016/j.precamres.2007.02.008.

Zhang, S.H., Zhao, Y., Liu, X.C., Liu, D.Y., Chen, F., Xie, L.W., Chen, H.H., 2009. Late Paleozoic to Early Mesozoic mafic-ultramafic complexes from the northern North China Block: Constraints on the composition and evolution of the lithospheric mantle. Lithos 110, 229–246. https://doi.org/10.1016/j.lithos.2009.01.008.

Zhang, H.F., Ying, J.F., Tang, Y.J., Li, X.H., Feng, C., Santosh, M., 2011. Phanerozoic reactivation of the Archean North China Craton through episodic magmatism: Evidence from zircon U–Pb geochronology and Hf isotopes from the Liaodong Peninsula. Gondwana Res. 19, 446–459. https://doi.org/10.1016/j.gr.2010.09.002.

Zhang, S.H., Li, Z.X., Evans, D.A.D., Wu, H.C., Li, H., Dong, J., 2012a. Pre-Rodinia supercontinent Nuna shaping up: a global synthesis with new paleomagnetic results from North China. Earth Planet. Sci. Lett. 353, 145–155. https://doi.org/10.1016/j.epsl.2012.07.034.

Zhang, S.H., Zhao, Y., Santosh, M., 2012b. Mid-Mesoproterozoic bimodal magmatic rocks in the northern North China craton: Implications for magmatism related to breakup of the Columbia supercontinent. Precambr. Res. 222–223, 339–367. https://doi.org/10.1016/j.precamres.2011.06.003.

Zhang, Z.J., Kusky, T., Gao, M., Cheng, Q.M., 2023. Spatio-temporal analysis of detrital zircon U-Pb geochronology and Hf isotope data: tests of tectonic models for the Precambrian evolution of the North China Craton. Earth Sci. Rev. 239, 104372. https://doi.org/10.1016/j.earscirev.2023.104372.

Zhao, G.C., Zhai, M.G., 2013. Lithotectonic elements of Precambrian basement in the North China Craton: Review and tectonic implications. Gondw. Res. 23, 1207–1240. https://doi.org/10.1016/j.gr.2012.08.016.

Zhao, G.C., Wilde, S.A., Cawood, P.A., Sun, M., 2001. Archean blocks and their boundaries in the North China Craton: lithological, geochemical, structural and P–T path constraints and tectonic evolution. Precambr. Res. 107 (1), 45–73. https://doi.org/10.1016/S0301-9268(00)00154-6.

Zhao, G.C., Cawood, P.A., Wilde, S.A., Sun, M., 2002. Review of the global 2.1–1.8 Ga orogens: Implications for a pre-Rodinian supercontinent. Earth Sci. Rev. 59 (1–4), 125–162. https://doi.org/10.1016/s0012-8252(02)00073-9.

Zhao, G.C., Sun, M., Wilde, S.A., Li, S.Z., 2005. Late Archean to Paleoproterozoic evolution of the North China craton: Key issues revisited. Precambr. Res. 136 (2), 177–202. https://doi.org/10.1016/j.precamres.2004.10.002.

Zhao, G.C., Shuwen, L., Sun, M., Sanzhong, L., Wilde, S., Xia, X., Zhang, J., He, Y., 2006. What happened in the Trans-North China Orogen in the period 2560-1850 Ma? Acta Geologica Sinica-English Edition 80 (6), 790–806. https://doi.org/10.1111/j.1755-6724.2006.tb00303.x.

Zhao, R., Guo, J., Peng, P., Liu, F., 2011. 2.1 Ga crustal remelting event in Hengshan complex: evidence from zircon U-Pb dating and Hf-Nd isotopic study on potassic granites. Acta Petrol. Sin. 27 (6), 1607–1623 (in Chinese with English abstract).

Zhao, G.C., Cawood, P.A., Li, S., Wilde, S.A., Sun, M., Zhang, J., He, Y., Yin, C., 2012. Amalgamation of the North China craton: Key issues and discussion. Precambr. Res. 222–223, 55–76. https://doi.org/10.1016/j.precamres.2012.09.016.

Zhao, J.H., Zhou, M.F., Wu, Y.B., Zheng, J.P., Wang, W., 2019. Coupled evolution of Neoproterozoic arc mafic magmatism and mantle wedge in the western margin of the South China Craton. Contrib. Miner. Petrol. 174, 4. https://doi.org/10.1007/s00410-019-1573-7.

Zheng, Y.F., 2019. Subduction zone geochemistry. Geosci. Front. 10, 1223–1254. https://doi.org/10.1016/j.gsf.2019.02.003.

Zheng, J.P., Griffin, W.L., O'Reilly, S.Y., Lu, F., Wang, C., Zhang, M., Wang, F., Li, H., 2004. 3.6 Ga lower crust in central China: New evidence on the assembly of the North China craton. Geology 32 (3), 229–232. https://doi.org/10.1130/G20133.1.

Zhong, Y., Kusky, T., Wang, L., Polat, A., Liu, X.Y., Peng, Y.Y., Luan, Z.K., Wang, C.H., Wang, J.P., Deng, H., 2021. Alpine-style nappes thrust over ancient North China continental margin demonstrate large Archean horizontal plate motions. Nat. Commun 12, 6172. https://doi.org/10.1038/s41467-021-26474-7.

Zhou, J.S., Yang, Z.S., Hou, Z.Q., Wang, Q., 2020. Amphibole-rich cumulate xenoliths in the Zhazhalong intrusive suite, Gangdese arc: Implications for the role of amphibole fractionation during magma evolution. Am. Mineral. 105, 262–275. https://doi.org/10.2138/am-2020-7199.

Zhu, T.C., Wang, Z.W., Wang, Z.H., Sun, Y.X., Liu, Z.Y., Xu, Y., Yu, J.W., Wei, H., Geng, X.J., 2022. Formation of late Paleoproterozoic Gaositai Hornblendite in Northern North China Craton: evidence from Zircon U-Pb Isotopes and Amphibole Trace elements. Minerals 12 (8), 1046. https://doi.org/10.3390/min12081046.

Zhu, R.Z., Smith, D.J., Wang, F., Qin, J.F., Zhang, C., Zhao, S., Liu, M., Zhang, F., Zhu, Y., Lai, S.C., 2024. Hornblendites as a record of differentiation, metasomatism and magma fertility in arc crust. Chem. Geol. 650, 121974. https://doi.org/10.1016/j.chemgeo.2024.121974.

Zindler, A., Hart, S.R., 1986. Chemical geodynamics. Annu. Rev. Earth Planet. Sci. 14, 493–571. https://doi.org/10.1146/annurev.ea.14.050186.002425.